






Article

Development of Bioinspired Functional Chitosan/Cellulose Nanofiber 3D Hydrogel Constructs by 3D Printing for Application in the Engineering of Mechanically Demanding Tissues

Arnaud Kamdem Tamo ^{1,2,3}, Ingo Doench ^{1,2,3}, Lukas Walter ^{1,2,3}, Alexandra Montembault ⁴ , Guillaume Sudre ⁴ , Laurent David ⁴ , Aliuska Morales-Helguera ⁵, Mischa Selig ⁶, Bernd Rolauuffs ⁶ , Anke Bernstein ⁶, Daniel Hoenders ⁷, Andreas Walther ⁷ and Anayancy Osorio-Madrado ^{1,2,3,*} 

- ¹ Laboratory for Sensors, Institute of Microsystems Engineering IMTEK, University of Freiburg, 79110 Freiburg, Germany; arnaud.kamdem@imtek.uni-freiburg.de (A.K.T.); ingo.doench@imtek.uni-freiburg.de (I.D.); lukas.walter@imtek.uni-freiburg.de (L.W.)
- ² Freiburg Materials Research Center—FMF, University of Freiburg, 79104 Freiburg, Germany
- ³ Freiburg Center for Interactive Materials and Bioinspired Technologies—FIT, University of Freiburg, 79110 Freiburg, Germany
- ⁴ Ingénierie des Matériaux Polymères IMP UMR 5223—CNRS, Université Claude Bernard Lyon 1, Université de Lyon, CEDEX, 69622 Villeurbanne, France; alexandra.clayer-montembault@univ-lyon1.fr (A.M.); guillaume.sudre@univ-lyon1.fr (G.S.); laurent.david@univ-lyon1.fr (L.D.)
- ⁵ Chemical Bioactive Center CBQ, Molecular Simulation and Drug Design Group, Central University of Las Villas, Santa Clara 50400, Cuba; aliuska@uclv.edu.cu
- ⁶ Center for Tissue Replacement, Regeneration & Neogenesis—G.E.R.N., Department of Orthopedics and Trauma Surgery, University of Freiburg, 79108 Freiburg, Germany; mischa.selig91@gmail.com (M.S.); berndrolauuffs@googlemail.com (B.R.); anke.bernstein@uniklinik-freiburg.de (A.B.)
- ⁷ Department of Chemistry, University Mainz, 55128 Mainz, Germany; daniel.hoenders@uni-mainz.de (D.H.); andreas.walther@uni-mainz.de (A.W.)
- * Correspondence: anayancy.osorio@imtek.uni-freiburg.de; Tel.: +49-761-203-67363



Citation: Kamdem Tamo, A.; Doench, I.; Walter, L.; Montembault, A.; Sudre, G.; David, L.; Morales-Helguera, A.; Selig, M.; Rolauuffs, B.; Bernstein, A.; et al. Development of Bioinspired Functional Chitosan/Cellulose Nanofiber 3D Hydrogel Constructs by 3D Printing for Application in the Engineering of Mechanically Demanding Tissues. *Polymers* **2021**, *13*, 1663. <https://doi.org/10.3390/polym13101663>

Academic Editor: Ki Hyun Bae

Received: 1 May 2021

Accepted: 17 May 2021

Published: 20 May 2021

Publisher's Note: MDPI stays neutral with regard to jurisdictional claims in published maps and institutional affiliations.



Copyright: © 2021 by the authors. Licensee MDPI, Basel, Switzerland. This article is an open access article distributed under the terms and conditions of the Creative Commons Attribution (CC BY) license (<https://creativecommons.org/licenses/by/4.0/>).

Abstract: Soft tissues are commonly fiber-reinforced hydrogel composite structures, distinguishable from hard tissues by their low mineral and high water content. In this work, we proposed the development of 3D printed hydrogel constructs of the biopolymers chitosan (CHI) and cellulose nanofibers (CNFs), both without any chemical modification, which processing did not incorporate any chemical crosslinking. The unique mechanical properties of native cellulose nanofibers offer new strategies for the design of environmentally friendly high mechanical performance composites. In the here proposed 3D printed bioinspired CNF-filled CHI hydrogel biomaterials, the chitosan serves as a biocompatible matrix promoting cell growth with balanced hydrophilic properties, while the CNFs provide mechanical reinforcement to the CHI-based hydrogel. By means of extrusion-based printing (EBB), the design and development of 3D functional hydrogel scaffolds was achieved by using low concentrations of chitosan (2.0–3.0% (*w/v*)) and cellulose nanofibers (0.2–0.4% (*w/v*)). CHI/CNF printed hydrogels with good mechanical performance (Young's modulus 3.0 MPa, stress at break 1.5 MPa, and strain at break 75%), anisotropic microstructure and suitable biological response, were achieved. The CHI/CNF composition and processing parameters were optimized in terms of 3D printability, resolution, and quality of the constructs (microstructure and mechanical properties), resulting in good cell viability. This work allows expanding the library of the so far used biopolymer compositions for 3D printing of mechanically performant hydrogel constructs, purely based in the natural polymers chitosan and cellulose, offering new perspectives in the engineering of mechanically demanding hydrogel tissues like intervertebral disc (IVD), cartilage, meniscus, among others.

Keywords: hydrogel 3D printing; polymer composites; chitosan; cellulose nanofibers; X-ray synchrotron scattering; micromechanics; tissue engineering

1. Introduction

There is an increasing interest in the development of 3D complex functional architectures with appropriate biomaterials and cells, in particular with the strategy of mimicking the cellular microenvironment of native tissues. Three-dimensional printing has emerged as a powerful tool for tissue engineering, which applies additive manufacturing to bio-fabricate 3D tissue-resembling objects with a high degree of spatial organization [1,2]. A layer-by-layer deposition of materials [1], called (bio)inks, is performed in specifically designed 3D shapes [3–5]. It can potentially impact patient care through fabrication of tissue substitutes for implantation and regeneration, or for drug and toxicity screening [6]. Engineering of polymer biomaterials with controlled microstructure approaching tissue functionalities, while serving as model to investigate cell behavior in more relevant 3D mimicking environments, is challenging [7]. The biomaterial and the cell types are key components, which can also impact the biofabrication process [8,9]. The development of bioinks, with good printability and bioactive properties, controlling cellular fate, still needs to be improved in order to advance the translation into the clinic. In a first step, to provide the proper physical, chemical, and biological cues to the cells, bioprinting of biocompatible biomaterials needs to be finely studied, since they directly act on cellular adhesion, differentiation, and proliferation. Three-dimensional scaffolds with interconnected pore network microstructures have been widely studied and shown to ensure cell viability and colonization and the diffusion of nutrients [10,11]. Before scaffold formation, (bio)ink characteristics should include appropriate viscosity, printability, biocompatibility, enhanced cell adhesion, mechanical performance, and, finally, biodegradability, if desired. A relatively limited number of biopolymer hydrogels are available as bioinks. Among them, the alginate-based systems are the most investigated ones [12], which have been tested for viability of fibroblasts, stem cells, chondrocytes, osteogenic activity support, neural tissue construction, etc. [13]. Nevertheless, alginate does not bind strongly with cells, often leading to improper cellular interactions. In vivo, it may induce strong inflammatory response and is relatively fast biodegraded. Gelatin is also commonly used due to its mild physical gelation triggered by temperature change [14]. Hydrogels of collagen, gelatin modified with methacrylate moieties, agarose, chitosan, carboxymethylchitosan, polycaprolactone (PCL), silk fibroin, hyaluronic acid (HA) [15,16], have been 3D printed, even with cellulose nanofibers [17], but not all of them were fabricated for tissue engineering applications.

There are three main methodologies used for 3D bioprinting: inkjet, extrusion-based, and light-assisted bioprinting. Microextrusion (EBB) can be performed with a broad viscosity range of dispensable materials by using inexpensive setups [18,19]. Depending on ink and plotting device, thin lines of ink with a width range from around 45 to 1200 μm can be printed by EBB. Liquids with low to very high viscosity (until around 10^7 mPa.s) are reported to be printable via extrusion. Specially, the polymer ink needs to be in “liquid” phase prior to extrusion to avoid nozzle clogging, and must gel very fast after extrusion, to become a stable 3D free-standing object. Thus, not all biomaterials are printable by EBB. In this work, EBB is the method of choice to fabricate mechanically performant 3D fiber-reinforced hydrogel constructs only constituted of natural compounds like chitosan and cellulose, without biopolymer modification or addition of any chemical crosslinker, for a vast range of applications in tissue engineering.

In view of the exceptional properties of chitosan hydrogels for tissue engineering [20–25], we propose here the 3D printing of bioinspired functional chitosan (CHI) hydrogels filled with non-modified cellulose nanofibers (CNF). Soft tissues like the intervertebral discs, skin, among others, are commonly complex fiber-reinforced hydrogel composites [21,22,26,27]. Chitosan is a family of chitin-derived cationic polysaccharides, consisting of β -(1-4)-glucosamine and *N*-acetyl-glucosamine units [28–33]. It exhibits excellent biological properties like biocompatibility, biodegradability, bacteriostaticity, and fungistaticity, and promotes wound healing, cell proliferation, tissue repair [21,22,25,34–38]. Cellulose is the main component of plant biomass and most abundant biopolymer worldwide. Its chains naturally form a highly crystalline structure (namely cellulose I allomorph), assem-

bled into microfibrils [39–43]. The unique crystalline properties of the processed native cellulose nanofibrils, combined with their high aspect ratio and renewability, have placed the cellulose nanofibers (CNF) as a green nanoreinforcement alternative for the design of environmentally friendly and high mechanical performance composites [39,44–46]. Specially, the nano/microfibrillated cellulose (MFC) can be produced from the peeling of the native fibers into a network of hairy fibrils [47–49]. As a nanomaterial, the question on CNF toxicity and environmental impact has been addressed [22]. Low toxicity has been reported, according to ecotoxicological, cytotoxicity and proinflammatory response studies [50–52]. Cellulose nanofibers have also been proposed for drug delivery systems [53], reinforcement for biomaterials [21,22,54–56], protein immobilization [57], etc. In hydrogel biomaterials, the use of CNFs is promising—in addition to their mechanical performance, CNFs form a network with high water retention, they are biocompatible and can yield transparent biomaterials [21,22,54,58]. Besides, cellulose nanofibers can be oriented within hydrogels. Osorio et al. [39] performed pioneer works where cellulose whisker nanocrystals were oriented in bulk polysaccharide hydrogel matrices by uniaxial stretching under controlled humidity, to yield anisotropic hydrogels.

The goal of this work is the development by microextrusion of bioinspired mechanically performant fiber-reinforced 3D hydrogel scaffolds, of completely natural polymers like chitosan, without any chemical crosslinking to achieve its gelation, and using as nanoreinforcement non-modified cellulose nanofibers, which hydrogel composites should find application in the engineering of mechanically demanding hydrogel tissues like intervertebral disc (IVD) [21,22,59,60], cartilage, meniscus, etc. Different natural polymers have been explored in hydrogel biomaterials to design provisional supports for regeneration/repair of intervertebral disc and cartilaginous tissues; among them, collagen [61], hyaluronic acid (HA) and its derivatives [61–64], chondroitin sulfate [64], agarose [65], alginate [66], chitosan and its derivatives [21,22,25], cellulose and its derivatives [21,22,67]. Doench et al. [21,22] prepared bulk chitosan hydrogels reinforced with CNFs for the regeneration and repair of both the *annulus fibrosus* (AF) and the *nucleus pulposus* (NP) regions of the intervertebral disc. They concluded that the addition of CNF significantly improves the mechanical properties of the composite hydrogels. Moreover, the in situ gelation of the CHI/CNF precursor viscous suspension could be used as non-invasive injectable applications in disc nucleosupplementation [22]. Additionally, they carried out ex vivo experiments in porcine models, also evidencing that the implantation of CHI/CNF composite hydrogels within fenestrated (defective) discs helps to restore their biomechanics [21,22]. Specially, the performance for *annulus fibrosus* (AF) tissue repair of distinct hydrogels based on HA, chondroitin sulfate, collagen has been evaluated in vivo applying rabbit, porcine, or bovine models [61–64]. Although hydrogels implantation has been related to an upregulation of extracellular matrix (ECM) genes such as Col1, Col2, and Decorin and catabolic matrix metalloproteases MMP13 and MMP3, nucleotomy, and implant administration resulted in localized annular damage with AF inflammation and scarring, impairing a proper tissue regeneration [61]. Therefore, other strategies focused on keeping disc integrity, preventing AF damage and NP reherniation. In this context, treatment of the *nucleus pulposus* with a liquid HA-based implant was proposed, which aimed to fill irregularly shaped defects through in situ polymerization yielding a strain resistant hydrogel [63]. A comparable approach investigated a minimal invasive shape-memory *annulus fibrosus* closing device of poly(D,L-lactide-co-trimethylene carbonate) (PLA-TMC) that revealed an elastic modulus of 1.7–2.5 MPa, ranging in the modulus of human AF tissue [68]. In conclusion, there is increasing interest in designing a non-inflammatory, mechanically performant, and well-integrated hydrogel for intervertebral disc repair, possibly with AF tissue sealing capacity, to ensure long-term regeneration of the IVD while preventing further degeneration.

In this work, the interest of cellulose is to ensure the mechanical performance needed in the pre-gelation state to deposit free-standing hydrogel constructs, while achieving fiber-filled bioinspired hydrogel biomaterials. The development strategy was based on

three main factors to obtain printable formulations: viscosity adjustment; ink flow prior to extrusion, and printed material-specific gelation and mechanical performance. In terms of nomenclature, it is worth noticing that the name “bioink” sometimes is used, as referred to the achievement of 3D printed hydrogel constructs for cell seeding and growing, even if biological bodies themselves were not directly incorporated in the initial ink. Different CHI/CNF ink compositions will be considered in this work. To evaluate the suitability of the 3D printed CHI/CNF hydrogel constructs for tissue engineering, cell growth and migration will be evaluated in 3D cell culture studies. The CHI/CNF composition and processing parameters will be optimized in terms of 3D printability and good quality of constructs (microstructure and mechanics), resulting in good cell viability.

2. Materials and Methods

2.1. Chitosan Source and Characterization

Chitosan from squid pen chitin was supplied by Mahtani Chitosan (Veraval, India; Batch type 144). The chitosan degree of acetylation (DA) was determined by ^1H NMR spectroscopy following the methodology of Hirai et al. [69,70]. The measurement was performed on a Bruker ALS 300 spectrometer (Bruker GmbH, Ettlingen, Germany) (300 MHz for ^1H) at 298 K, which revealed a low DA of 2.5%. The CHI molecular weight was determined by size exclusion chromatography (SEC) coupled to multiangle laser light scattering (MALLS) at the Chromatography Center of Institute of Chemistry of Lyon (ICL) [70–73]. To this end, chitosan solutions at 0.1% (*w/v*) were prepared in an acetic acid/ammonium acetate buffer pH = 4.5 (AcOH (0.2 M)/AcONH₄ (0.15 M)), which was used as an eluent. Then, they were filtered through 0.45 μm pore size membranes (Millipore, Merck KGaA, Darmstadt, Germany). The chromatographic equipment was composed of an IsoChrom LC pump (Spectra-Physics, Santa Clara, CA, USA) connected to a Protein Pack 200 SW (Waters GmbH, Eschborn, Germany) column and a TSK gel G6000 PWXL. A multiangle laser light scattering detector DAWNDSP (Wyatt Technology Europe GmbH, Dernbach, Germany), operating at 632.8 nm, was coupled online to a WATERS 410 differential refractometer. The chitosan number (Mn) and weight-average molecular weights (Mw) determined by SEC/MALLS were 4.10×10^5 g/mol ($\pm 6.4\%$) and 6.11×10^5 g/mol ($\pm 9.6\%$), respectively, which yield a polydispersity index $I_p = M_w/M_n = 1.49$ ($\pm 11.6\%$).

2.2. Cellulose Nanofibers

The used cellulose nanofiber type was nanofibrillated cellulose. Cellulose nanofiber (CNF) suspensions were obtained from bleached pine sulfite dissolving pulp at the Centre Technique du Papier (CTP, Grenoble, France), by a mechanoenzymatic method adapted from Pääkkö et al. [74]. Before 1 h incubation at 50 °C with a solution of endoglucanase FiberCare R[®] (Novozyme, Bagsvaerd, Denmark) at pH 5.0, the pulp was refined at 4.5% consistency with a 12" single disk refiner for 25 min. The digested samples were further refined to obtain a pulp suspension of Schopper-Riegler (SR) number higher than 80 SR and mean fiber length lower than 300 μm . Fiber suspensions at 2% (*w/w*) were collected with an Ariete homogenizer (Montigny le Bretonneux, France), involving one pass at 1000 bar, followed by 3 passes at 1500 bars. The obtained CNFs displayed a surface charge density of 40–80 mmol/kg and were weakly charged with carboxylate moieties.

2.3. Transmission Electron Microscopy

Morphology and dimensions of the cellulose nanofibers were investigated by transmission electron microscopy (TEM). Drops of a 0.001% (*w/v*) CNF suspension were deposited on carbon coated copper grids (CF400-CU Carbon Film, 400 Mesh Copper grids), which were previously cleaned with plasma to get rid of surface contamination and make the grid more adhesive towards the sample. The samples were negatively stained with 2% (*w/v*) uranyl acetate in suspension. Then, samples were allowed to dry and were observed in the TEM microscope, model Zeiss LEO 912 Omega (Carl Zeiss Microscopy GmbH, Jena, Germany), operating at 80 kV.

2.4. Preparation of Chitosan/Cellulose Nanofiber Viscous Inks

Chitosan (CHI) viscous solutions: A stoichiometric amount of acetic acid was added to chitosan powder dispersed in MilliQ water, as to protonate the free amine groups present in the glucosamine units of chitosan (accounting for a chitosan degree of acetylation (DA) value of 2.5%) and thereby allow the CHI complete solubilization. The mixture was left under mechanical stirring overnight. Chitosan aqueous solutions at 2%, 3%, and 4% (*w/v*) were prepared, named as CHI2, CHI3, and CHI4 formulations, respectively.

Cellulose nanofiber-filled CHI viscous suspensions: The CHI powder was firstly mixed with CNFs aqueous suspension in MilliQ water and the dispersions were sonicated with a SONOPULS Ultrasonic homogenizer (Bandelin electronic GmbH, Berlin, Germany) for 5 min at 40% amplitude. Then, a stoichiometric amount of acetic acid was added to completely solubilize the CHI contained in the mixture. The obtained suspension was mechanically stirred overnight to ensure a good dispersion of CNFs within the CHI solution. Viscous ink formulations, with CHI concentration of 2%, 3%, or 4% (*w/v*) and cellulose nanofibers (CNF) contents of 0.4%, 0.5%, or 0.6% (*w/v*) were obtained.

Rheological Behavior

A rotational rheometer AR-2000 (TA Instruments, New Castle, DE, USA) fitted with a cone and a plate flow geometry was used to characterize the rheological behavior of the CHI/CNF viscous inks at 25 °C, with a gap size of 116 µm and a solvent trap to prevent its drying or evaporation. The cone-plate geometry (25 mm diameter; 4°) allows one to ensure a uniform shearing to the sample. The analysis was performed in triplicate in the continuous mode in a shear rate range from 0.005 to 1000 s⁻¹ and the equilibrium time was set at 15 s. TA Instruments TRIOS software was used in the measurements. Finally, the flow diagrams of the CHI/CNF ink formulations were obtained, namely the plots of the steady-state shear viscosity vs. shear rate.

2.5. 3D Printing of Cellulose Nanofiber-Filled Chitosan Hydrogel Scaffolds

The 3D printing of scaffolds of chitosan/cellulose nanofibers hydrogels was performed with the 3D-Discovery Evolution bioprinter device (RegenHU, Villaz-St-Pierre, Switzerland), consisting of an x–y–z-axis positioning system with a tool changer equipped with several printhead stations, and a building platform. The 3D structures were printed using a CAD software controlled xyz motion-system that guides the tip position. Multilayer square-shaped porous CHI/CNF hydrogel structures were 3D printed by microextrusion using a pressure controlled direct-ink-writing system.

After preparing the inks as above (i.e., CHI solutions and CHI/CNF suspensions) they were centrifuged for 20 min at 2000 rpm, to eliminate air bubbles before microextrusion. In the 3D-Discovery bioprinter, the inks were loaded in a syringe (Nordson EFD, Feldkirchen, Germany) mounted in a dispensing adaptor and extruded through precision conic dispense tips with inner diameter of 250 or 410 µm (Nordson EFD, Feldkirchen, Germany), with a printing speed of 40 mm·s⁻¹ under applying a given pressure (0.15–0.77 bar). Scaffolds were shaped as nets of 30 × 30 mm² in size, composed by the alternation of 4 orthogonal layers, each constituted of parallel hydrogel filaments printed with 0.85 mm interspace. Hydrogel scaffolds were directly printed in Petri dishes containing aqueous 2 M NaOH for chitosan neutralization, which was used as coagulation bath. The distance between the extrusion needle tip and the Petri dish surface was set at 3 mm, by using a calibration laser integrated to the 3D-Discovery Evolution bioprinter device. After a neutralization time of 15 min, scaffolds were taken out from the alkaline bath and washed several times with MilliQ water until neutrality. Chitosan/cellulose nanofiber hydrogel filaments and 3D scaffolds were printed using the above protocol with ink formulations containing CHI at a concentration of 2 or 3% (*w/v*), and a CNF content of 0.4% (*w/v*). Table 1 summarizes the varied CHI/CNF ink compositions with the different inner diameters (ID) of the extrusion needles and extrusion pressure used in the direct-ink-writing process in the bioprinter device.

Table 1. Processing parameters for the printing of hydrogel filaments and 3D hydrogel scaffolds of CHI/CNF formulations.

Formulation	CHI % (w/v)	CNFs % (w/w)	Needle Inner Diameter ID (μm)	Extrusion Pressure (bar)
F1 (CHI2)	2	0	410	0.15
F2 (CHI2/CNF0.4)	2	0.4	410	0.25
F3 (CHI3)	3	0	410	0.35
F4 (CHI3/CNF0.4)	3	0.4	410	0.47
F5 (CHI2)	2	0	250	0.25
F6 (CHI2/CNF0.4)	2	0.4	250	0.35
F7 (CHI3)	3	0	250	0.70
F8 (CHI3/CNF0.4)	3	0.4	250	0.77

2.5.1. Scanning Electron Microscopy

The freeze-dried CHI/CNF printed hydrogel scaffolds were carefully fractured and gold sputtered in a Polaron SC 7640 (VG Microtech, East Sussex, UK), and observed by scanning electron microscopy (SEM) (Amray Inc., Bedford, MA, USA) at an accelerating voltage of 15 kV. It is worth noticing that with this technique the analysis was performed in the freeze-dry state. Nevertheless, it allowed to get insight into the dispersion of the CNFs in the dry scaffold composites, which were originated from the hydrogel processing.

2.5.2. Microtensile Testing

The hydrogels of all CHI/CNF ink formulations shown in Table 1 were printed in a single horizontal layer with an interspace of 2 mm, to characterize the hydrogel filament resolution and mechanical properties. These latter were investigated using a microtensile testing device. Hydrogel filaments were cautiously cut by using a razorblade to obtain a length of approximately 8 mm. The cut filaments were glued onto a foliar frame with a test span of about 7 mm by using cyanoacrylate glue (Loctite® 454, Henkel AG & Co, Munich, Germany). Tests were conducted under controlled relative humidity (RH) of 45%, at a constant crosshead displacement speed of 8 $\mu\text{m/s}$, and the applied force (F) was measured by a load cell with a maximum capacity of 50 N. The nominal stress σ was calculated as the ratio of the applied force F to the initial cross sectional area A of the hydrogel filament ($\sigma = F/A$), and the nominal strain ε was expressed as the ratio of the extension of the hydrogel filament respect to its initial length l_0 ($\varepsilon = \Delta l/l_0 = (l - l_0)/l_0$). The Young's modulus (E), ultimate stress (σ_b), and strain at break (ε_b) were determined from the obtained stress–strain curves, considering at least six measurement replicates ($n = 6$) for each printed formulation.

2.5.3. Wide and Small-Angle X-ray Synchrotron Scattering (WAXS and SAXS). In Situ Microtensile Testing

X-ray synchrotron scattering analyses were performed at the microfocus beamline mySpot, BESSY II at the Helmholtz-Zentrum Berlin HZB (Germany) and at the beamline BM02/D2AM at the European Synchrotron Radiation Facility ESRF (Grenoble, France). At Bessy II, data were collected at a wavelength $\lambda = 1.0 \text{ \AA}$, which setup allowed simultaneously measuring small (SAXS) and wide-angle X-ray scattering (WAXS) using a two-dimensional MARCCD detector. At this microfocus beamline, the synchrotron X-ray beam had a diameter of around 10 μm , which passed through the CHI/CNF printed hydrogel filament placed in a holder with Kapton foil windows, allowing for in situ tensile testing of the hydrogel biomaterial while recording SAXS and WAXS signals. At the ESRF, SAXS data were collected at a wavelength $\lambda = 0.78 \text{ \AA}$ using a CCD detector (Roper Scientific GmbH, Ottobrunn, Germany). Both at Bessy II and at the ESRF, the silver behenate was used as standard to calibrate the scattering vector q -range, and transmission corrections and background subtraction were performed in the SAXS/WAXS data treatment.

2.6. 3D Cell Culture of Fibroblasts in the Printed Hydrogel Scaffolds

To evaluate the suitability of the CNF/CHI 3D printed hydrogels for tissue engineering, fibroblast cells were cultured in the 3D hydrogel scaffolds, as 3D printed and washed, without any hydrogel drying step before cell cultivation. Cultures of 3T3 cells developed using the NIH Swiss mouse embryo fibroblasts were performed (murine fibroblast, strain: NIH/Swiss). Cells were grown in T75 (75 cm²) cell culture flasks (Sarstedt, Nümbrecht, Germany). The cells were cultured in Dulbecco's modified Eagle medium (DMEM) supplemented with 2 mM L-glutamine and 10% fetal bovine serum (FBS) (Gibco, Thermo Fisher Scientific, Leicestershire, UK) at 37 °C in a humidified atmosphere of 5% CO₂ for 1 week. Upon 90% confluence, cells were rinsed twice with phosphate-buffered saline (PBS) (Gibco, Thermo Fisher Scientific, Leicestershire, UK) followed by detachment with trypsin/ethylene diamine tetra acetic acid (EDTA) for 5 min and neutralization with the corresponding cell culture medium. After detachment, cells were spun down in a centrifuge for 5 min at 110 rcf (Rotor F-45-30-11, Eppendorf 5417R, Hamburg, Germany). The supernatant was discarded and cells were diluted into the culture medium. The 3D printed CHI/CNF hydrogel scaffolds were put in 6-well cell culture plates, covering the whole well surface for subsequent use for cell growth. To this end, 500 µL of suspension of the cells in culture medium as above were added on the 3D printed CHI/CNF hydrogel scaffolds, considering a starting loading average of 10⁵ cells per well. The NIH/3T3 fibroblasts seeded in triplicate in scaffolds of different CHI concentrations and CNF contents were kept at 37 °C in CO₂ incubation. Cells seeded in empty wells (i.e., without 3D-printed hydrogels) were used as a control.

Live/Dead Cell Viability Assay

The viability of the cells was qualitatively evaluated to get an indication of whether fibroblasts survive and grow in the CHI/CNF hydrogel scaffolds. Cultivation of at least 6 days was possible and proliferation was observed. The cells were inspected for viability by fluorescent staining with a live/dead staining kit: calcein AM/ethidium-homodimer-1, LIVE/DEAD™ viability/cytotoxicity kit, (Thermo Fisher Scientific, Leicestershire, UK). After 1, 3, and 6 days of cell culture in the 3D hydrogel scaffolds as described above, a cell washing step was performed with Hank's balanced salt solution (HBSS, Gibco, Thermo Fisher Scientific, Leicestershire, UK) and the freshly prepared LIVE/DEAD solution was added to each sample. Samples were kept at incubation conditions for 15 min. After staining, the wells were imaged using a confocal laser-scanning microscope (Leica TCS SPE, Wetzlar, Germany). As the LIVE indicator, calcein AM marks cell cytoplasm in green fluorescence; and as the DEAD indicator, ethidium homodimer-1 stains cell nucleus in red fluorescence.

Cell counting: Image analysis of the LIVE/DEAD cell viability assay micrographs was performed with Fiji (v1.52u), an ImageJ-based program [75]. Images were converted to 8-bit and the contrast was normalized via 'histogram normalization' command. The trainable weka segmentation tool was then used for cell segmentation [76]. Cells were counted using the Fiji "find maxima" command with a constant noise level to distinguish cell maxima vs. background noise. The results were exported to Excel for further statistical analyses.

Statistical analysis: All cell counting data were expressed as mean ± standard deviation (SD). Statistical analysis was performed by the one-way analysis of variance (ANOVA) using the software STATISTICA 10.0 (StatSoft Inc: Tulsa, OK, USA, 2011), followed by the Tukey's HSD post hoc test if significant differences were found ($p < 0.05$) in the ANOVA.

3. Results and Discussion

3.1. Cellulose Nanofibers Microstructure

Figure 1 shows TEM micrographs and the X-ray diffraction pattern of the cellulose nanofibers (CNF) used to produce the CNF-filled chitosan inks and printed scaffolds. The CNFs consisted of an entangled network of interconnected nanofibrils with very high aspect ratio (length/width), with an average width of 35.2 ± 8.1 nm and bundles of up

to around 50 nm width. The relatively high value of this latter could be related to the drying during TEM sample preparation, which might induce partial fibril aggregation [74]. The mechanoenzymatic hydrolysis used to produce the nanofibers yields long nanofibrils preserving the native cellulose I crystalline allomorph structure, as displayed in the X-ray diffraction pattern (Figure 1c), with partly amorphous regions, which are able to inherently entangle and form a fibril network with hairy branches [74]. The preserved native cellulose I allomorph and the intramolecular hydrogen bonding within amorphous and crystalline phases can lead to efficient nanoreinforcement effect, above from fibers consisting of regenerated cellulose II allomorph.

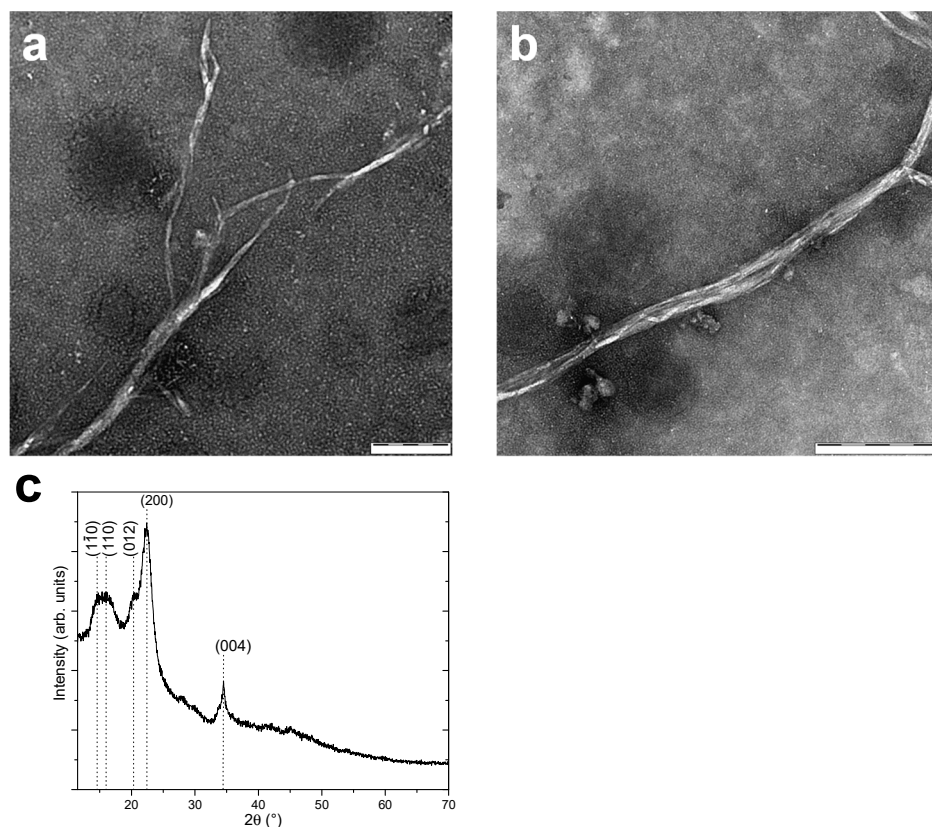


Figure 1. (a,b) TEM images of cellulose nanofibers (CNFs) at different magnifications. Scale bars: (a) 100 nm; (b) 200 nm. (c) Wide angle X-ray diffraction pattern of the CNFs, with indexed crystallographic planes of native cellulose I allomorph.

3.2. Chitosan/Cellulose Nanofiber Inks Rheological Behavior

Figure 2 shows the flow diagrams of the CNF-filled chitosan viscous suspensions and the corresponding chitosan solutions. A steady plateau corresponding to the Newtonian viscosity is observed for all characterized samples. Two distinct regions can be observed in the different curves: At low shear rates, the Newtonian flow region shows a constant zero-shear viscosity (η_0), as the provided shear forces to disentangle the polymer chains appear to be lower or equal to those maintaining them tangled; at higher shear rates, a shear-thinning behavior is observed with a decrease of viscosity as the shear rate increases [77,78].

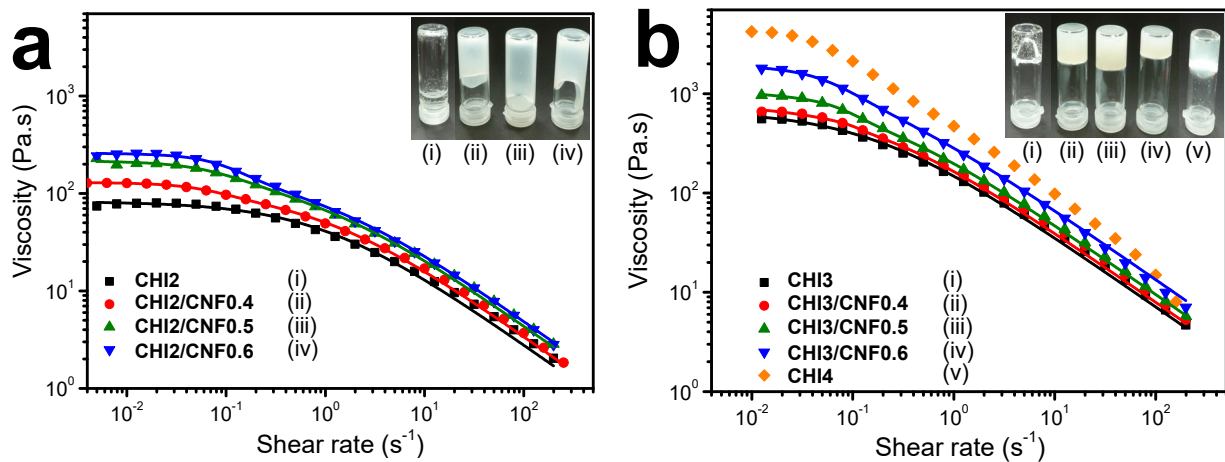


Figure 2. Flow diagrams of the CNF-filled CHI viscous inks (a) and the corresponding naked CHI inks (b). Solid lines represent the fitting of the rheological behavior with the Cross model equation (Equation (1)) for CHI solutions, and with the double Cross model equation (Equation (2)) for the CHI/CNF suspensions. Insets in show pictures of the different viscous inks.

The flow diagrams (η vs. $\dot{\gamma} = d\gamma/dt$) of the “pure” chitosan solutions (Figure 2) could be modelled with the three-parameter Cross law (Equation (1)): [79–81]

$$\eta = \frac{\eta_{0,CHI}}{1 + (\dot{\gamma}\tau_{CHI})^{1-n_{CHI}}} \quad (1)$$

The Cross equation yields the Newtonian or zero-shear viscosity η_0 , the flow behavior index n , and the relaxation time of chitosan polymer chains τ , as displayed in Table 2. As expected, the steady-state shear viscosity of the pure CHI inks increased with increasing CHI concentration. The polymer chain interactions and entanglements increased with the polymer concentration, restricting the chain relaxation into disentanglement. The CHI/CNF viscous inks exhibited more complex flow diagrams, with higher Newtonian viscosities measured in the low shear rate range ($\dot{\gamma} < 1 \text{ s}^{-1}$) and shear thinning occurring in two different regimes, which was more evident for higher CNF contents (Figure 2). Thus, these two-step flow diagrams of the CHI/CNF suspensions could be modelled with a double Cross law (Equation (2)):

$$\eta = s \frac{\eta_{0,CHI}}{1 + (\dot{\gamma}\tau_{CHI})^{p_{CHI}}} + \frac{\eta_{0,CNF}}{1 + (\dot{\gamma}\tau_{CNF})^{p_{CNF}}} \quad (2)$$

where $\eta_{0,CNF}$, τ_{CNF} , and $p_{CNF} = 1 - n_{CNF}$ are the flow parameters of CHI chains, possibly due to chains interacting with CNFs in the CHI/CNF suspensions in the slower flow regime. Rheological model fitting used a Levenberg–Marquardt nonlinear regression algorithm in the Octave 4.4.0 programming environment [22]. Table 2 shows the flow parameters obtained for the CHI/CNF suspensions and the Newtonian viscosity $\eta_{0,CHI}$, the relaxation time τ_{CHI} , and the exponent $p_{CHI} = 1 - n_{CHI}$ for pure CHI solutions. For a given chitosan concentration, the presence of CNF increased the Newtonian viscosity measured at low shear rates. With the increase of the shear rate, the viscosity of both the pure CHI viscous solutions and the CHI/CNF inks similarly decreased, revealing almost the same shear-thinning behavior. In the CHI/CNF formulations two different chain relaxation phenomena might occur. In the “pure” CHI inks, the main chain relaxation, being dominating at high shear rate and corresponding to the disentanglement of the polymer chains transient network, shows relaxation time of 1 s in inks with 2% (w/v) CHI, and around 6 s in inks with 3% (w/v) CHI (Table 2) [82,83]. At a low shear rate, in the presence of CNFs, a second relaxation occurs with relaxation times of the order of 10 s (practically independently of the CNF content, except for the formulation CHI3/CNF0.6

with the highest CHI and CNF concentrations). To conclude, the higher Newtonian viscosity measured at low shear rates in the CHI solutions filled with CNFs, in comparison to the pure CHI solutions, and their similar shear-thinning behaviors with similar flow exponents at high shear rates, could be explained due to the CHI polymer chain relaxation (disentanglements) impacted by the CHI concentration [84]. As mentioned above, the CNFs surface is weakly charged with carboxylate moieties displaying a surface charge density of 40–80 mmol/kg [85,86]. Weak electrostatic interactions could establish between the CHI polycation and the CNF polyanionic surface, allowing for stress transfer from the CHI solution matrix to the nanofibers. According to the results, in the CHI/CNF inks the establishment of a rigid cellulose network with permanent CNF–CNF interactions would not occur, as a gel-like flow behavior with $\eta \sim 1/\dot{\gamma}$ would be instead observed [87]. Actually, CHI chains could adsorb on the CNFs surface and play a role in the bridging of nanofibers [88,89], resulting in entanglements formation between the adsorbed chains and the other chains in the solution. Addition of the CNFs, even at low concentration, is likely to impact the dynamics of CHI chains since the surface area of the nanofibers is very large [58].

Thus, the relaxation time τ for chitosan is hypothesized to be interdependent with the incorporation of CNF. When adding the CNFs, the observed relaxation time τ_{CNF} can increase due to both the increase of CNF content and of CHI concentration (Table 2). Such relaxation time is tentatively related to the rupture of CNF/CHI network (CNF strands bridged by chitosan chains), which effect seems to be more important after reaching a threshold of CHI concentration beyond 2% (w/v). Increasing the CNF content should result in a denser CNF network, possibly involving rearrangements at larger scales of CNF aggregates. Then, higher CHI concentration also should contribute to the CNF/CHI network, since adsorbed CHI chain would act as fibril binders. It also will imply a denser network with longer relaxation times, associated with larger scale reorientation and interfibrillar bridge rupture with applied strains. Then, the decrease of the exponent p_{CNF} (Table 2) consistently should reflect a more heterogeneous CNF network disruption process at higher CNF contents, specially emphasized in systems with higher CHI concentration. Nevertheless, the study of the flow diagrams in the extended shear rate range, for example by capillary rheometry with use of the Weissenberg–Rabinowitsch correction as we previously investigated (Doench et al. [22]), would be necessary to determine the exponent parameter p with precision.

Table 2. Flow parameters determined from the viscosity vs. shear rate curves (Figure 2) of different CHI/CNF compositions, by using the Cross model (Equation (1)) for naked CHI inks and double Cross model (Equation (2)) for CHI/CNF formulations.

Formulation	$\eta_{0,CHI}$ (Pa·s)	τ_{CHI} (s)	p_{CHI}	s	$\eta_{0,CNF}$ (Pa·s)	τ_{CNF} (s)	p_{CNF}
CHI2	83	1.0	0.73	-	-	-	-
CHI2/CNF0.4	83	1.0	0.73	1.22	30.4	11.9	1.96
CHI2/CNF0.5	83	1.0	0.73	1.56	87.8	9.6	1.46
CHI2/CNF0.6	83	1.0	0.73	1.75	116.3	8.6	1.95
CHI3	674	6.0	0.71	-	-	-	-
CHI3/CNF0.4	674	6.0	0.71	1.11	39.3	8.7	6.55
CHI3/CNF0.5	674	6.0	0.71	1.33	207.3	10.9	2.87
CHI3/CNF0.6	674	6.0	0.71	1.88	752.1	13.9	1.89

Thus, the CHI/CNF inks flow at high shear rates is dominated by the CHI chains disentanglement and is less affected by the presence of the CNFs. This is advantageous for printability by extrusion of this system, as CNFs can contribute to improve mechanical properties and increase the zero shear viscosity while practically not affecting the extrudability of CHI-based systems (higher shear rates).

3.3. Cellulose Nanofiber-Filled Chitosan Printed Hydrogels

3.3.1. Morphology and Dimensions

Figure 3 shows images of hydrogel filaments printed from different CHI/CNF formulations by varying the extrusion needle inner diameter (ID) and pressure as displayed in Table 1. The addition of CNFs into the CHI viscous solutions slightly decreases the diameter of the printed hydrogel filaments. This might be related to a limited swelling at the die outlet due to the increased viscosity and relaxation time resulting from mild interaction between CHI and CNFs, as inferred from the rheological analysis. In general, the decrease of extrusion needle inner diameter offers an increase resolution of printed filaments [90]. Thus, the combined effect of the composition of the CHI/CNF formulation, needle inner diameter, and pressure contribute to the size resolution of the hydrogel filaments.

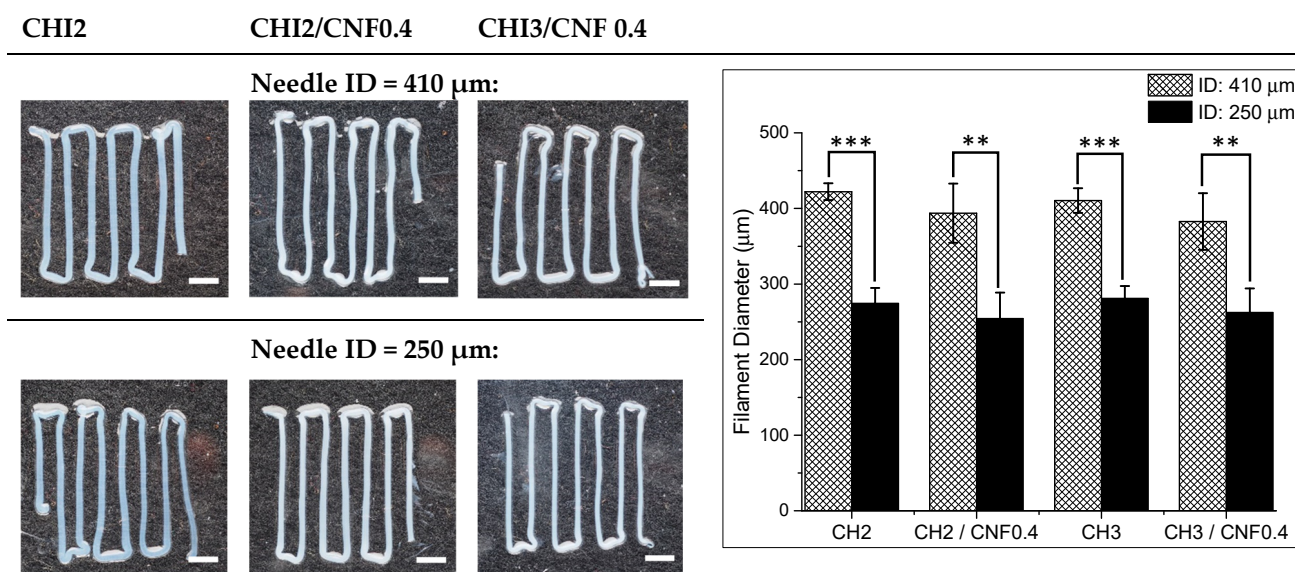


Figure 3. Photos of the hydrogel filaments obtained by microextruding CHI/CNF viscous suspensions of different compositions through needles with tip inner diameters (ID) of 250 or 410 μm (scale bars: 1500 μm). Histograms with hydrogel filament mean diameters obtained after printing the different CHI/CNF formulations. Right: Printed hydrogel average filament diameters obtained for the different CHI/CNF formulations, using the two different extrusion needle ID. For the statistical analysis, independent sample *t*-tests were performed with STATISTICA 10.0 (StatSoft Inc: Tulsa, OK, USA, 2011). $p < 0.05$ was accepted as statistically significant. Filament diameter values are expressed as means \pm SDs. $n = 6$ (** $p < 0.01$, *** $p < 0.001$).

Figure 4 shows scanning electron microscopy (SEM) micrographs of the cross-section of the CHI/CNF filaments after freeze-drying. Although the lyophilizates are known to exhibit a coarser morphology in comparison with hydrogels [91], the obtained scaffolds show a fine spider web-like network microstructure with interconnected fibrils, which might facilitate cell adhesion, proliferation, and migration. Cellulose nanofibers were not distinguishable, which should confirm a good dispersion of the CNFs in the composite. The SEM images revealed that with the increase in CHI concentration, the porosity decreases and the pore sizes strongly increases with the incorporation of CNFs (Figure 4). In one hand, the nanofibers seem to favor microstructures with more expanded flat walls with still residual fibrillar network morphology (Figure 4b). Sereni et al. [92] reported on the formation of radial capillaries or microrange tubular pores in CHI physical hydrogels, related to directional neutralization of chitosan chains during hydrogel processing. The addition of CNF has influence on CHI/CNF suspension viscosity, which should impact the size of resulting tubular pores in hydrogels [92]. Such tubular porosity revealed in related biopolymer hydrogels might be also observed in the freeze-dried scaffolds.

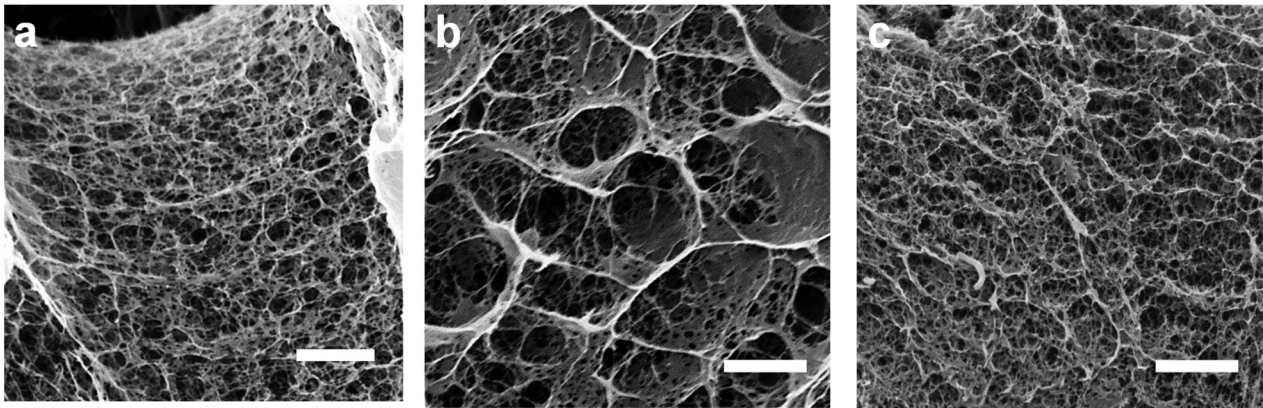


Figure 4. Scanning electron micrographs (SEM) of hydrogels printed from neat chitosan CHI 2% and 3% (*w/v*) ink formulations ((a,c), respectively), and from CHI2/CNF0.4 ink formulation (b). Scale bars: 5 μm .

3.3.2. Mechanical Properties

Figure 5 shows the stress–strain curves of microtensile testing performed on the printed CHI and CHI/CNF hydrogel filaments. Figure 5c summarizes the achieved Young’s modulus (E), stress (σ_b), and strain at break (ϵ_b) obtained for filaments of different compositions and printing conditions. The mechanical behavior was influenced by the CHI concentration, the CNFs content and the printing processing parameters like the extrusion needle inner diameter (ID). The Young’s modulus and tensile strength increased with the CHI and CNF concentrations, but decreased with the increase of needle inner diameter. As expected, varying CNFs concentrations from 0 to 0.4% induced a significant enhancement in the mechanical properties of composite hydrogel filaments. Finally, mechanical properties of CHI hydrogels could be improved by reinforcing with the CNFs. The enhanced properties are due to the CNFs nanoscale (large specific surface area), high Young’s modulus, and aspect ratio typical of nanofibrillated cellulose [21,22,42,43,56]. In the hydrogel composites, an efficient matrix/reinforcement interaction should contribute to the stress transfer from the CHI matrix to the nanofibers, thereby yielding higher stiffness and strength. Moreover, in the microtensile testing the uniaxial stretching was performed in the same direction as the axis of the extrusion needle. Thus, the obtained mechanical properties should be also impacted by the orientation of both the CHI polymer chains and the CNFs along the hydrogel extrudate axis, due to shear-induced orientation during extrusion. Such effect could be more significant when using a thinner extrusion needle like that of ID = 250 μm (Figure 5).

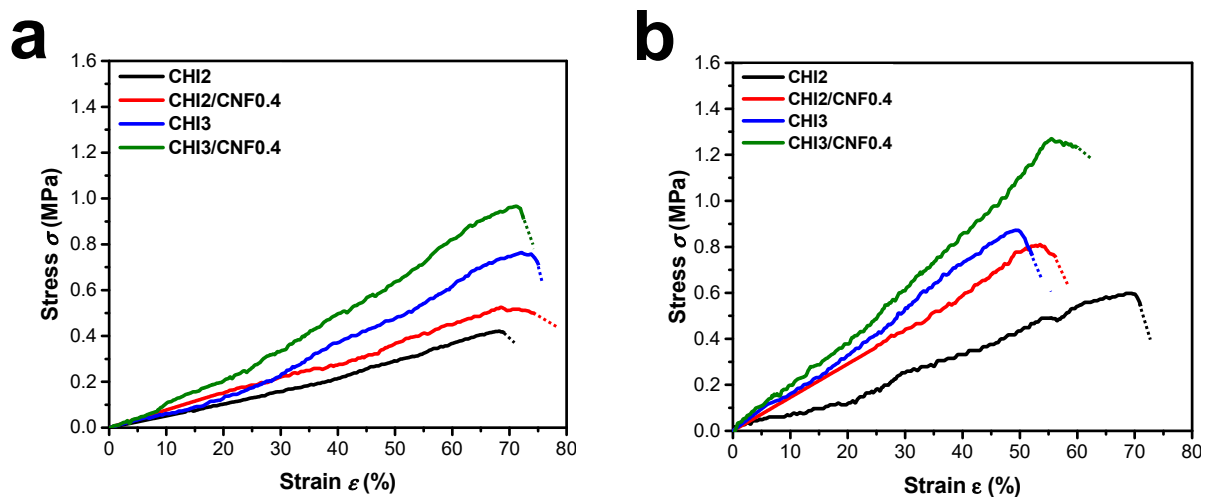


Figure 5. Cont.

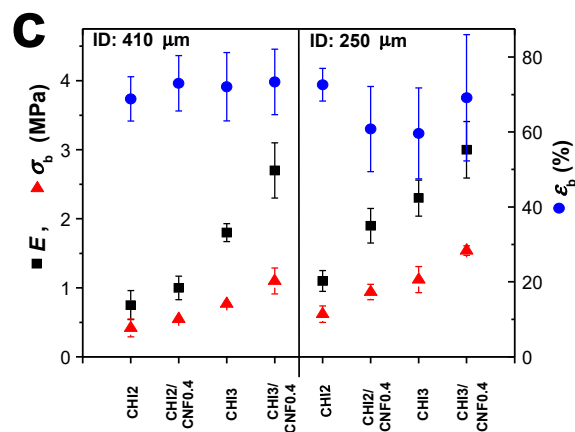


Figure 5. Stress–strain curves of uniaxially stretched printed hydrogel filaments of chitosan (CHI) alone and cellulose nanofiber (CNF) filled chitosan composites, for different CHI and CNF concentrations, by using conic extrusion needles with inner diameter (ID) of: (a) 410 μm and (b) 250 μm. (c) Young’s modulus (E), stress (σ_b), and strain at break (ϵ_b) achieved for the tensile tested filaments in (a,b), obtained with the two different extrusion needle IDs.

3.3.3. Synchrotron X-ray Scattering SAXS/WAXS Analyses of Printed Hydrogels. Characterization of the Cellulose Nanofibers Dispersion and Orientation

Microstructural characterization was also performed by synchrotron X-ray scattering SAXS and WAXS of the CHI/CNF printed hydrogel filaments. Figure 6a shows the SAXS analyses of printed CHI/CNF hydrogel composites and the corresponding CHI reference. In the low q -range (where $qR_0 \ll 1$, with R_0 being the radius of nanofibrillar objects), a scattering law between $1/q^2$ and $1/q^3$ was observed, closer to $1/q^2$ for the pure CHI hydrogel, and to $1/q^3$ for the CHI/CNF systems. This scattering laws could be attributed to a large distribution of cross-section radii R_0 of the fibril-like features constituting the hydrogel fibrillar network microstructure in pure CHI hydrogels [40,93], as revealed by SEM (Figure 4); and also to the morphology of the CNF rod-like particles with broad cross-sectional size distribution. In the q -range for $q > 0.7 \text{ nm}^{-1}$, the Porod’s law ($I(q) = C/q^4$) is evidenced, revealing the sharp electron density variation within the microstructure. The Porod’s law can be used to estimate the Porod’s length ($l_p = \frac{V_{CNF}}{S_{CNF}} \sim \frac{Q}{\phi_{CNF}\pi C}$) of the CNFs, where Q is the scattering invariant $Q = \int_0^\infty I(q)q^2 dq$, and C the Porod’s constant [94]. Then, the invariant Q can be estimated using the Equation (3), which is divided in three subintegrals (Q_1 , Q_2 , and Q_3) corresponding to integration in different regions of the SAXS scattering curve (Figure 6a): (Q_1) at the lowest (low- q Guinier region, $q \rightarrow 0$), (Q_2) middle (intermediate- q Guinier region) with q_{max} around 0.7 nm^{-1} , and (Q_3) final slope (Porod region) q -values, with the lowest q -angle SAXS trend of the regions (1) and (i2) mainly obtained by extrapolation.

$$Q = \int_0^\infty I(q)q^2 dq = \int_0^{q_{min}} Aq^{2+\alpha} dq + \sum_{q_{min}}^{q_{max}} I(q_i)q_i^2 \Delta q + \int_{q_{max}}^\infty \frac{C \cdot \exp(-s^2 q^2)}{q^2} dq \quad (3)$$

The Porod’s constant C was deduced by non-linear least square fit (using `lsqcurvefit()` function in Matlab). The approximate value of the Porod’s length l_p was expressed as $l_p \sim \frac{Q}{\pi C}$, with Q being the sum of the subintegrals Q_1 , Q_2 , and Q_3 . For example, from the SAXS curve of the formulation CHI3/CNF0.4, containing 3% (w/v) CHI and 0.4% (w/v) CNF, the resulted l_p value was $\sim 8 \text{ nm}$, which should correspond to the smallest width of the cellulose fibrils within the suspension. This fairly agrees with the width range of the individualized cellulose nanofibrils as observed by TEM (Figure 1a), demonstrating that

an excellent dispersion of the CNFs was obtained within the printed CNF-filled chitosan hydrogel composites.

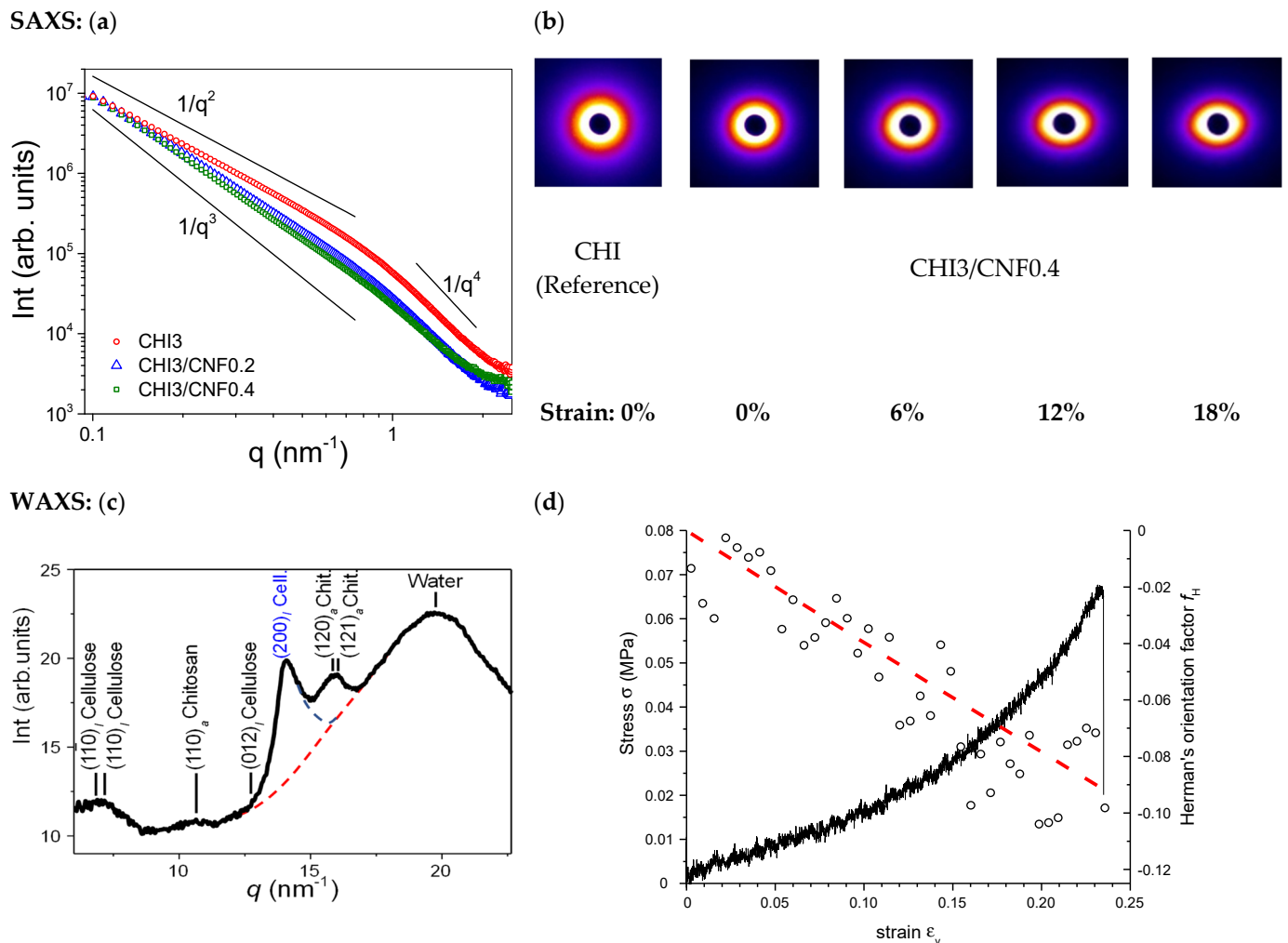


Figure 6. (a) Synchrotron small-angle X-ray scattering (SAXS) radial average curves of the CHI/CNF printed hydrogel filaments; (b) 2D SAXS image patterns recorded for different strains after stretching the CHI3/CNF0.4 printed hydrogel formulation, with printed CHI hydrogel reference included. (c) Synchrotron wide-angle X-ray scattering (WAXS) radial average of printed CHI3/CNF0.4 hydrogel composite, for example, after 14% of tensile strain; (d) Evolution of the Herman's orientation factor f_H estimated from the azimuthal intensity plots of the $(200)_I$ reflection of cellulose I (fitted with Lorentz function) at different strain values during in situ uniaxial stretching (rate: $1 \mu\text{m/s}$, RH: 45%) using X-ray synchrotron radiation, for the CHI3/CNF0.4 printed hydrogel. The red dashed-line in (d) shows the CNF orientation distribution function obtained by the affine model used for reorientation of rigid rod-like crystals [95,96].

Then, uniaxial stretching of the printed hydrogel filaments was performed at the synchrotron beamline to allow in situ microstructural characterization by X-ray scattering (SAXS/WAXS) and the orientation of the CNFs within the CHI/CNF hydrogels and its quantification (Figure 6a). The appearance of the SAXS patterns in Figure 6b (Right), which become more anisotropic when the strain values increased, shows that the preferential orientation of CNF and chitosan nanofibrils in the hydrogel biomaterial could be further increased at stretching the printed filaments. From the 2D WAXS synchrotron patterns of the CHI/CNF hydrogels, the Herman's orientation factor f_H of cellulose crystals could be calculated. To this end, the 2D X-ray scattering images were azimuthally sectorized, and the intensity peak around the $(200)_I$ crystallographic ring of Cellulose I allomorph was deconvoluted (Figure 6c) for each sector centered at the azimuthal angle φ_k . This

calculation was performed for different diffraction images obtained for different strain values (Figure 6d) during stretching the CHI/CNF hydrogel filament at the synchrotron X-ray beamline. From this $I_{200,k}$ sectorization, the Hermans' orientation factor for the (200)_I reflection of Cellulose I was obtained as follows (Equation (4)):

$$f_H = \frac{\int_{\varphi=0}^{360} I_{200}(\varphi) \cos^2(\varphi) \sin(\varphi) d\varphi}{\int_{\varphi=0}^{360} I_{200}(\varphi) \sin(\varphi) d\varphi} = \frac{\sum_{k \text{ sector}} I_{200,k} \cos^2(\varphi_k) \sin(\varphi_k) \Delta\varphi}{\sum_{k \text{ sector}} I_{200,k} \sin(\varphi_k) \Delta\varphi} \quad (4)$$

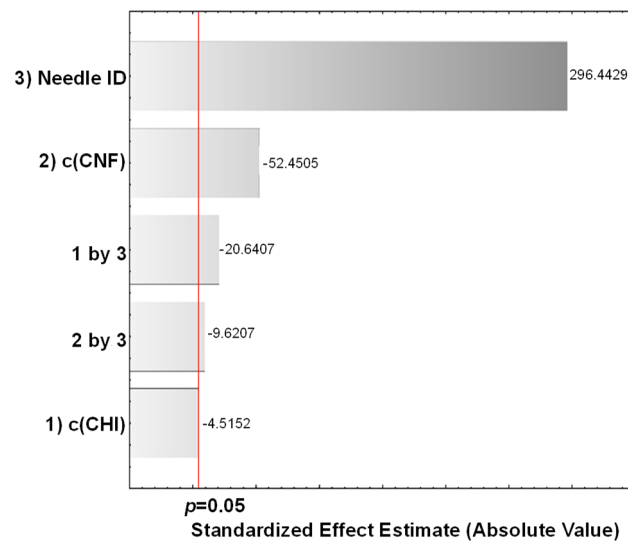
where $\Delta\varphi$ is the azimuthal angle differentiate for each sector. The details of the deconvolution fit with Lorentz functions and parabolic contribution of water, the treatment of the sector-averaged azimuthal intensity vs. azimuthal angle φ_k , and the resulting calculation of the $\langle \cos^2\varphi \rangle$ are described in the Supporting Information (Supplementary Materials Figure S1 and Equation (S2)). Figure 6d shows that the Hermans' orientation factor evolved from close to 0 (random orientation) to -0.11 (anisotropic orientation of CNF) at stretching the CHI3/CNF0.4 printed hydrogel till strain around 20%. For printed CHI3/CNF0.2 hydrogels, a similar decrease of f_H until down to -0.08 was obtained after a 20% applied strain (data not shown). The evolution of the f_H values confirms the enhancement of alignment of CNFs in the stretching axis, which enhances the mechanical performance of the hydrogel composites. The calculated values of Hermans' factor f_H due to CNF orientation are in good agreement with the affine model calculation [95,96] shown in Figure 6d (red) (see also Supplementary Materials Figure S1), describing the reorientation of rigid rod-like crystals.

3.3.4. Experimental Design for the Optimization of the Size Resolution and Mechanical Performance of CHI/CNF Printed Hydrogels

An experimental design allowed statistically evidencing the impact of the processing parameters discussed above on the printed hydrogel filament diameter and mechanical properties. To determine the most significant parameters affecting the resolution and mechanical performance of the printed CHI/CNF hydrogels, the three independent variables: concentration of chitosan $c(\text{CHI})$, cellulose nanofibers content $c(\text{CNF})$, and printing extrusion needle tip inner diameter (ID) were considered in the statistical analysis. As above, the $c(\text{CHI})$, $c(\text{CNF})$, and needle ID were varied following two levels: $c(\text{CHI})$: 2% and 3% (w/v); $c(\text{CNF})$: 0% and 0.4% (w/w); needle ID: 250 and 410 μm . A 2^3 factorial design was used, including the eight formulations described in Table 1. The run order of the experiments was randomized to prevent systematic errors. The following responses: printed CHI/CNF hydrogel filament diameter (Figure 3) and mechanical properties (Young's modulus E , and stress at break σ_b) (Figure 5) were evaluated with the analysis of variance (ANOVA) using the software STATISTICA 10.0 (StatSoft Inc: Tulsa, OK, USA, 2011). The significance of the effects was verified with Fisher's statistical test using 0.05 as significance level. ANOVA analyses showed that the CNFs content and the needle ID were the most significant variables ($p < 0.05$) influencing on the diameter of the printed hydrogel filaments. Concerning mechanical properties, the three factors: (1) $c(\text{CHI})$; (2) $c(\text{CNF})$; (3) needle ID were significant for the Young's modulus and the stress at break of the printed filaments. Interactions of $c(\text{CHI})$ *needle ID (1 by 3) and of $c(\text{CNF})$ *needle ID (2 by 3) also have significant influence on the filament diameter. The ANOVA results are shown in Supplementary Materials Tables S1–S3 while Pareto Charts are depicted in Figure 7. The needle ID has the strongest effect on the hydrogel filament diameter. As expected, a thinner needle leads to smaller filament diameters. The $c(\text{CNF})$ has a negative effect on this response, which means that higher $c(\text{CNF})$ is needed to achieve thinner filaments. The interaction between $c(\text{CHI})$ and needle ID (1 by 3) also has a negative effect on the filament diameter. When the needle ID is in its lower level (250 μm), the $c(\text{CHI})$ also should be in its lower level (2% (w/v)) in order to reach the lowest filament diameter. Similarly, if the needle ID is in its higher level (410 μm), a high $c(\text{CHI})$ is preferred to develop filaments with smaller diameter. These

effects are shown in Supplementary Materials Figure S2. For the mechanical properties, the $c(\text{CHI})$ and $c(\text{CNF})$ have positive effect, while needle ID has a negative one. Thus, higher Young's modulus and stress at break are achieved for higher concentrations of CHI, CNF, and smaller needle ID. Finally, as both responses are important to achieve printable and functional CHI/CNF hydrogel filaments of high size resolution and good mechanical properties, which might be a premise for the 3D printing of hydrogel constructs, the desirability function was used to simultaneously optimize the two responses (filament diameter and mechanical properties). This function is based on a numerical interval that defines the desirability of the analyst in relation to the process optimal condition. To achieve hydrogel filaments with the lowest diameter and the highest mechanical performance, the optimization using the desirability function yielded as optimum processing parameters: $c(\text{CHI}) = 3\%$ (w/v); $c(\text{CNF}) = 0.4\%$ (w/w); needle ID = 250 μm (Supplementary Materials Figure S3), corresponding to that used in the formulation F8 of Table 1.

a) Hydrogel filament diameter



b) Young's modulus E (Stiffness)

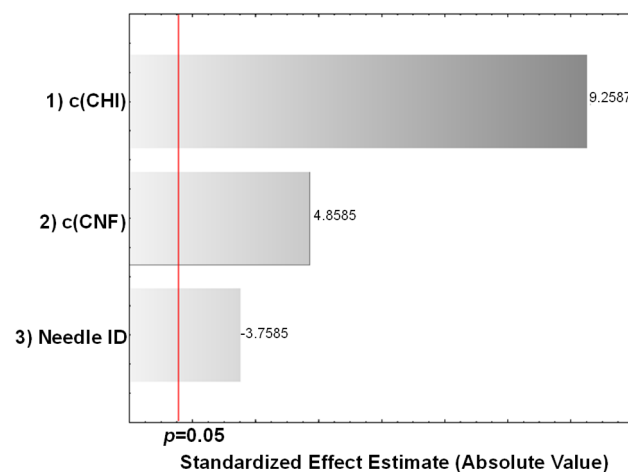


Figure 7. Cont.

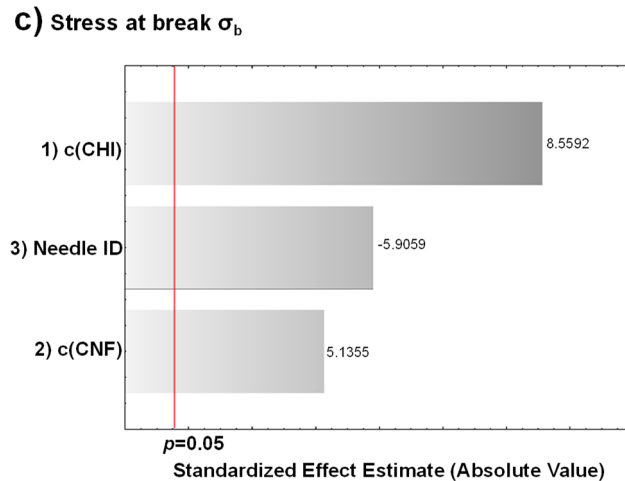


Figure 7. Pareto chart of the three responses: (a) hydrogel filament diameter, (b) Young's modulus E , and (c) stress at break σ_b , after considering a two level variation of the variables: (1) $c(\text{CHI})$, (2) $c(\text{CNF})$, and (3) needle ID, in a 2^3 factorial experimental design.

3.4. 3D Printed CHI/CNF Hydrogel Scaffolds

The obtained good conditions for hydrogel filament resolution and mechanical properties were considered for the printing of hydrogel scaffolds and in vitro cell culture experiments. The 3D scaffolds of varied CHI and CNF concentrations were printed for comparison, and with the different needle IDs, to demonstrate the feasibility of extending the above results into printing approaches in 3D, in the form of layered hydrogels. Again, the benefit of adding CNFs as reinforcement in CHI hydrogels to print 3D CHI/CNF hydrogel composites was clearly observed, where 3D CHI-based scaffolds of both 2% and 3% (w/v) chitosan containing CNFs amount as low as 0.4% showed lower filament diameter, i.e., better resolution than those scaffolds only containing chitosan (Figure 8).

Needle ID: 410 μm

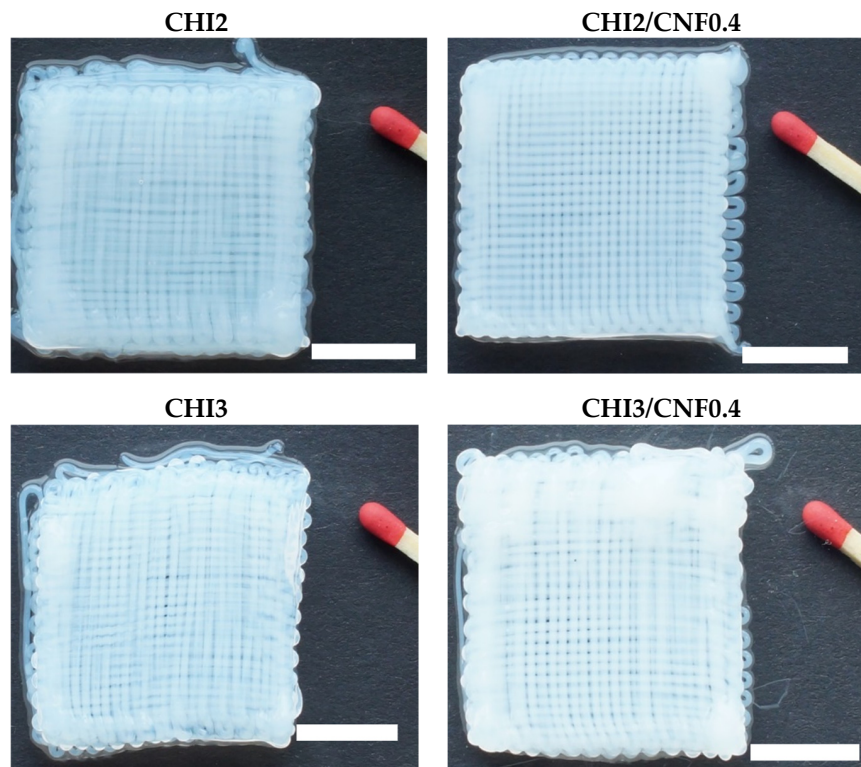


Figure 8. *Cont.*

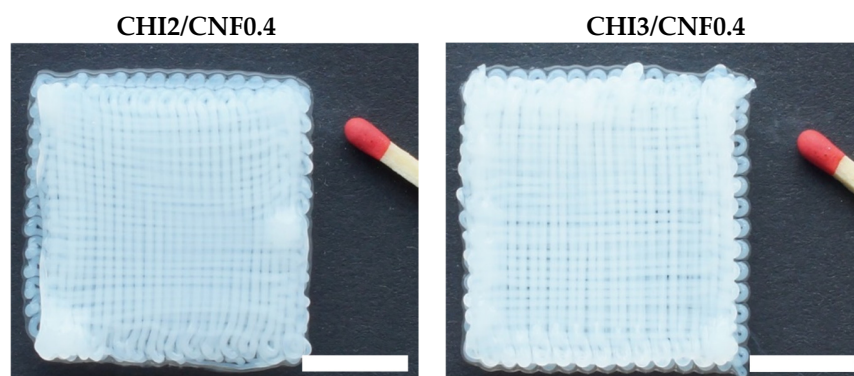
Needle ID: 250 μm 

Figure 8. The 3D printed scaffolds of chitosan/cellulose nanofiber hydrogels with $30 \times 30 \text{ mm}^2$ and 0.85 mm interfilament distance. Scale bars: 11.5 mm.

Suitability of 3D Printed CHI/CNF Hydrogel Scaffolds for Three-Dimensional Cell Culture

NIH/3T3 fibroblast cells were cultured in the printed multilayer CHI/CNF hydrogels. Three different ink formulations (CHI2, CHI3, and CHI2/CNF0.4) were considered in the cell culture studies. LIVE/DEAD cell viability assays at Day 1, 3, and 6 were performed. Figure 9a shows micrographs obtained at the confocal fluorescent microscope for different scaffold compositions at the corresponding culture times.

Cells proliferated within the accessible interfilament spaces predefined for the printed multilayer hydrogel mesh, which yielded cellularized bioconstructs. For the lower CHI concentration (2% (*w/v*)), after initial cell adhesion on the filaments surface, the cells also colonized the inner microstructure of the hydrogel filaments as clearly observed after days 3 and 6 for the CHI2 and for the CHI2/CNF0.4 formulations (Figure 9). This was hardly observed in the mesh printed with CHI 3% (*w/v*), which might be related to a lower porosity of the hydrogel filaments at higher CHI concentrations (as displayed in the SEM observation of corresponding lyophilizates, Figure 4c), which might hinder cell colonization in the denser hydrogel. This led to significant cell death after 6 days of incubation in the CHI3 formulation. In contrast, for scaffolds prepared with CHI 2% (*w/v*), which in addition contained 0.4% of CNFs, an appreciable colonization of cells was observed both in the inner porous microstructure of the CHI2/CNF0.4 hydrogel filaments and in the interspaces (big pores) of the scaffold mesh with dimensions predetermined in the 3D printing process. Thus, fluorescent micrographs after 3 and 6 days of culture in the CHI2/CNF0.4 constructs display a growing of cells in 3D, which becomes more significant and homogeneous after 6 days (Figure 9). The incorporation of CNFs at that low content of 0.4% (*w/v*), in hydrogels prepared with low CHI concentration like 2% (*w/v*), seems to phenomenologically yield the appropriate composition for the best *in vitro* response, which related microstructure is displayed in the SEM analysis of Figure 4b in comparison to the other compositions. The achieved pore sizes combination, the inner walls surface of the composite microstructure and the mechanical properties (Young's modulus: 2 MPa, stress at break: 1 MPa) of this CHI2/CNF0.4 composition seems to be optimal for cell adhesion and proliferation with guaranteed nutrients exchange in the 3D hydrogel scaffold, resulting in homogeneous cell colonization within the whole scaffold (Figure 9). Thus, the addition of CNFs to CHI improves hydrogel stiffness and does not compromise the biocompatibility of chitosan and viability of cells.

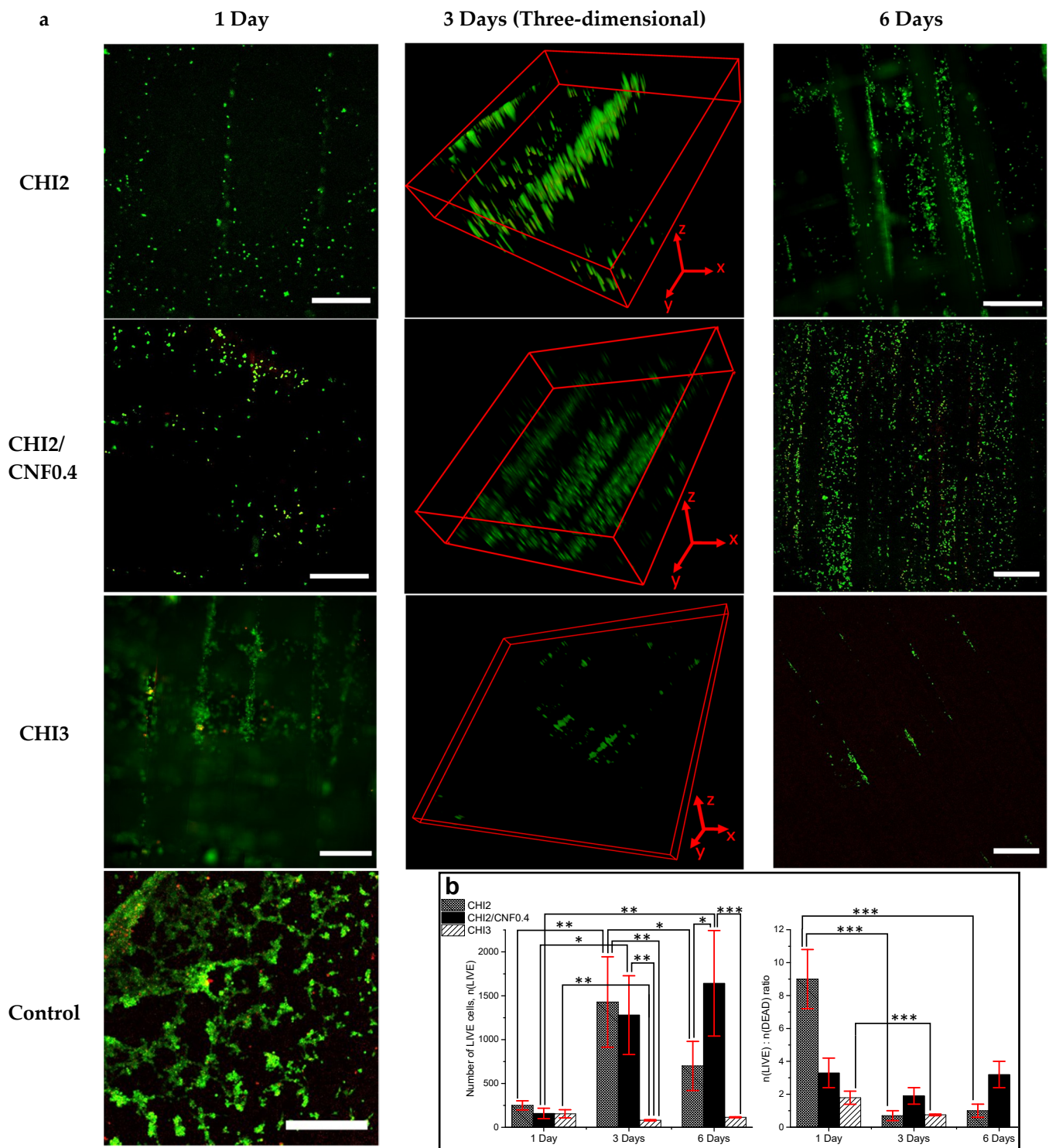


Figure 9. (a) LIVE/DEAD assay confocal laser scanning microscopy (CLSM) images after culture of NIH/3T3 fibroblast cells in 3D printed CHI/CNF hydrogel composite scaffolds of different CHI and CNF concentrations (Figure 8). LIVE indicator: green fluorescence; DEAD indicator: red fluorescence. Scale bars: 500 μ m. Three-dimensional frames (3 days) scale: CHI2 $x*y*z$: 2.3*2.3*0.075 mm³; CHI2/CNF0.4 $x*y*z$: 2.3*2.3*0.50 mm³; CHI3 $x*y*z$: 3.0*3.0*0.15 mm³. (b) (Left) Number of LIVE cells $n(LIVE)$; (Right) $n(LIVE)/n(DEAD)$ cell ratio obtained for the different CHI/CNF formulations at the different days, expressed as means \pm SDs, $n = 4$ (* $p < 0.05$, ** $p < 0.01$, *** $p < 0.001$).

The above findings were quantitatively evaluated and demonstrated in the statistical analysis of the LIVE and DEAD counted cells (see also Supporting Information).

Figure 9b reports the number of LIVE cells counted after 1, 3, and 6 days of culture of fibroblasts within the 3D printed hydrogel scaffolds containing different concentrations of CHI and CNFs. Between the different formulations, after 3 days significant differences were observed in the number of living cells with more alive cells in the formulations containing low chitosan concentration like the CHI2 and CHI2/CNF0.4, respect to the CHI3 hydrogel scaffold; and with no significant differences in the number of living cells between those formulations of low chitosan concentration (CHI2 and CHI2/CNF0.4). Then, after 6 days incubation, the number of living cells in the cellulose nanofiber-filled chitosan hydrogel was significantly higher than in the scaffolds prepared with chitosan alone (Figure 9b). The ratio of living to dead cells $n(\text{LIVE}):n(\text{DEAD})$ was also statistically evaluated (Figure 9b) and significant differences were observed in the CHI2 and CHI3 formulations for the days 3 and 6 with respect to day 1, this is with a significant increase of the number of dead cells after day 3. In contrast, in the formulation containing the cellulose nanofibers (CHI2/CNF0.4) the balance between LIVE and DEAD cells did not significantly change along the considered culture days.

4. Conclusions

The engineering of purely natural and mechanically performant bioinspired 3D printed hydrogels, for application in tissue engineering, of chitosan (CHI) hydrogels filled with cellulose nanofibers (CNFs) without any modification of the biopolymer constituents and addition of any chemical crosslinker, was achieved by extrusion-based 3D printing technology. The addition of cellulose nanofibers with high mechanical properties into chitosan hydrogel ensured good printing ability and printed constructs resolution without compromising chitosan bioactivity and biocompatibility. The viscosity of the printable CHI/CNF suspensions (inks) was as low as $100\text{--}500\text{ Pa}\cdot\text{s}$ at shear rate 1 s^{-1} and allowed the deposition of gel filaments of good mechanical performance and printing resolution ($220\text{--}430\text{ }\mu\text{m}$). Stable 3D hydrogel meshes were obtained with very low concentration both of the biopolymer matrix and the nanofiber filler, still supporting three-dimensional cell colonization and good cell viability, yielding cellularized bioconstructs. Finally, the most relevant CHI/CNF biomaterial technical characteristics were optimized to produce natural bioinspired 3D functional fiber-filled hydrogels for tissue engineering applications with great potential in the repair of mechanically demanding hydrogel tissues like intervertebral disc, cartilage, meniscus, among others. The immediate perspective of this work is the development of different 3D-shape bioconstructs, targeting the anisotropic and multilamellar hydrogel structure of intervertebral disc regions. This will constitute a forward step of our previous studies dedicated to assess biocompatible and functional composite hydrogel implants in disc tissue engineering and regeneration, with the advantage of using 3D printed more-mimicking hydrogel environments for cell and tissue growth.

5. Patents

Osorio-Madrado, A.; David, L.; Montembault, A.; Viguier, E.; Cachon, T. Hydrogel Composites Comprising Chitosan and Cellulose Nanofibers. International Patent Application No. WO 2019/175279 A1, 19 September 2019; US Patent App. 16/980,383, 12 February 2021.

Supplementary Materials: The following are available online at <https://www.mdpi.com/article/10.3390/polym13101663/s1>, Figure S1: Azimuthal intensity around the diffraction signal (200)₁ of cellulose I crystals constituting the cellulose nanofibers (CNFs) vs. azimuthal angle φ ; Figure S2: Effect of the interaction between $c(\text{CHI})$ and needle ID on the hydrogel filament diameter; Figure S3: Profiles of predicted values and desirability; Table S1: ANOVA analysis for printed hydrogel filament diameter, Table S2: ANOVA analysis for Young's modulus E of printed hydrogel filament, Table S3: ANOVA analysis for stress at break of printed hydrogel filament.

Author Contributions: Conceptualization, A.O.-M.; methodology, A.K.T., I.D., L.W., A.M., G.S., L.D., M.S., B.R., A.B., D.H., A.W., and A.O.-M.; investigation, A.K.T., I.D., L.W., A.M., G.S., L.D., M.S.,

and A.O.-M.; writing—original draft preparation, A.K.T. and A.O.-M.; writing—review and editing, A.K.T., L.D., A.M.-H., and A.O.-M.; supervision, A.O.-M.; funding acquisition, A.O.-M. All authors have read and agreed to the published version of the manuscript.

Funding: This research was funded by the Emmy Noether Programme of the German Research Foundation DFG (Grant number: OS 497/6-1). We thankfully acknowledge the financial support from Helmholtz-Zentrum Berlin HZB for the synchrotron X-ray scattering SAXS/WAXS beamtime allocated for measurements at Bessy II (Berlin, Germany). The article processing charge (APC) was funded by the Baden-Wuerttemberg Ministry of Science, Research and the Arts (MWK) and the University of Freiburg in the funding program Open Access Publishing.

Institutional Review Board Statement: Not applicable.

Informed Consent Statement: Not applicable.

Data Availability Statement: Not applicable.

Acknowledgments: We thank the Emmy Noether Programme of the German Research Foundation DFG (Grant number: OS 497/6-1) for funding. A.K.T. thanks the German Academic Exchange Service (DAAD) for financial support. We would like to thank Ivo Zizak for assistance during the synchrotron X-ray scattering experiments at the microfocus mySpot beamline at Bessy II, HZB (Berlin, Germany). We thank the French CRG Group for the synchrotron experiments carried out at the European Synchrotron Radiation Facility ESRF (Grenoble, France) and Cyrille Rochas for assistance during the experiments at the BM02/D2AM synchrotron beamline. We thank Agnès Crépet and the efforts of the Plateforme de Chromatographie ICL—IMP, France, Barbara Enderle, Elke Stibal, Ralph Thomann, and Yi Thomann for technical assistance. We thank Gerald Urban and Marie-Pierre Laborie for their collaboration.

Conflicts of Interest: The authors declare no conflict of interest.

References

1. Gensler, M.; Leikeim, A.; Möllmann, M.; Komma, M.; Heid, S.; Müller, C.; Boccaccini, A.R.; Salehi, S.; Groeber-Becker, F.; Hansmann, J. 3D printing of bioreactors in tissue engineering: A generalised approach. *PLoS ONE* **2020**, *15*, e0242615. [[CrossRef](#)] [[PubMed](#)]
2. Parra-Cantu, C.; Li, W.; Quiñones-Hinojosa, A.; Zhang, Y.S. 3D bioprinting of glioblastoma models. *J. 3D Print. Med.* **2020**, *4*, 113–125. [[CrossRef](#)] [[PubMed](#)]
3. Yan, Y.; Chen, H.; Zhang, H.; Guo, C.; Yang, K.; Chen, K.; Cheng, R.; Qian, N.; Sandler, N.; Zhang, Y.S.; et al. Vascularized 3D printed scaffolds for promoting bone regeneration. *Biomaterials* **2019**, *190–191*, 97–110. [[CrossRef](#)] [[PubMed](#)]
4. Ying, G.; Jiang, N.; Parra-Cantu, C.; Tang, G.; Zhang, J.; Wang, H.; Chen, S.; Huang, N.; Xie, J.; Zhang, Y.S. Bioprinted Injectable Hierarchically Porous Gelatin Methacryloyl Hydrogel Constructs with Shape-Memory Properties. *Adv. Funct. Mater.* **2020**, *30*, 2003740. [[CrossRef](#)] [[PubMed](#)]
5. Li, H.; Cheng, F.; Li, W.; Cao, X.; Wang, Z.; Wang, M.; Robledo-Lara, J.A.; Liao, J.; Chávez-Madero, C.; Hassan, S.; et al. Expanding sacrificially printed microfluidic channel-embedded paper devices for construction of volumetric tissue models in vitro. *Biofabrication* **2020**, *12*, 045027. [[CrossRef](#)] [[PubMed](#)]
6. Apsite, I.; Constante, G.; Dulle, M.; Vogt, L.; Caspari, A.; Boccaccini, A.R.; Synytska, A.; Salehi, S.; Ionov, L. 4D Biofabrication of fibrous artificial nerve graft for neuron regeneration. *Biofabrication* **2020**, *12*, 035027. [[CrossRef](#)]
7. Heid, S.; Boccaccini, A.R. Advancing biopinks for 3D bioprinting using reactive fillers: A review. *Acta Biomater.* **2020**, *113*, 1–22. [[CrossRef](#)]
8. Zhu, W.; Ma, X.; Gou, M.; Mei, D.; Zhang, K.; Chen, S. 3D printing of functional biomaterials for tissue engineering. *Curr. Opin. Biotechnol.* **2016**, *40*, 103–112. [[CrossRef](#)]
9. Malda, J.; Visser, J.; Melchels, F.P.; Jüngst, T.; Hennink, W.E.; Dhert, W.J.A.; Groll, J.; Huttmacher, D.W. 25th Anniversary Article: Engineering Hydrogels for Biofabrication. *Adv. Mater.* **2013**, *25*, 5011–5028. [[CrossRef](#)]
10. Hsu, S.-H.; Hung, K.-C.; Chen, C.-W. Biodegradable polymer scaffolds. *J. Mater. Chem. B* **2016**, *4*, 7493–7505. [[CrossRef](#)]
11. Ma, P.X. Biomimetic materials for tissue engineering. *Adv. Drug Deliv. Rev.* **2008**, *60*, 184–198. [[CrossRef](#)] [[PubMed](#)]
12. Hazur, J.; Detsch, R.; Karakaya, E.; Kaschta, J.; Tessmar, J.; Schneidereit, D.; Friedrich, O.; Schubert, D.W.; Boccaccini, A.R. Improving alginate printability for biofabrication: Establishment of a universal and homogeneous pre-crosslinking technique. *Biofabrication* **2020**, *12*, 045004. [[CrossRef](#)] [[PubMed](#)]
13. Park, J.; Lee, S.J.; Chung, S.; Lee, J.H.; Kim, W.D.; Lee, J.Y.; A Park, S. Cell-laden 3D bioprinting hydrogel matrix depending on different compositions for soft tissue engineering: Characterization and evaluation. *Mater. Sci. Eng. C* **2017**, *71*, 678–684. [[CrossRef](#)] [[PubMed](#)]

14. Skardal, A.; Devarasetty, M.; Kang, H.-W.; Mead, I.; Bishop, C.; Shupe, T.; Lee, S.J.; Jackson, J.; Yoo, J.; Soker, S.; et al. A hydrogel bioink toolkit for mimicking native tissue biochemical and mechanical properties in bioprinted tissue constructs. *Acta Biomater.* **2015**, *25*, 24–34. [[CrossRef](#)]
15. Derakhshanfar, S.; Mbeleck, R.; Xu, K.; Zhang, X.; Zhong, W.; Xing, M. 3D bioprinting for biomedical devices and tissue engineering: A review of recent trends and advances. *Bioact. Mater.* **2018**, *3*, 144–156. [[CrossRef](#)]
16. Hauptstein, J.; Böck, T.; Bartolf-Kopp, M.; Forster, L.; Stahlhut, P.; Nadernezhad, A.; Blahetek, G.; Zernecke-Madsen, A.; Detsch, R.; Jüngst, T.; et al. Hyaluronic Acid-Based Bioink Composition Enabling 3D Bioprinting and improving quality of deposited cartilaginous extracellular matrix. *Adv. Health Mater.* **2020**, *9*, 2000737. [[CrossRef](#)] [[PubMed](#)]
17. Gladman, A.S.; Matsumoto, E.A.; Nuzzo, R.G.; Mahadevan, L.; Lewis, J.A. Biomimetic 4D printing. *Nat. Mater.* **2016**, *15*, 413–418. [[CrossRef](#)] [[PubMed](#)]
18. Ravanbakhsh, H.; Bao, G.; Luo, Z.; Mongeau, L.G.; Zhang, Y.S. Composite inks for extrusion printing of biological and biomedical constructs. *ACS Biomater. Sci. Eng.* **2020**. [[CrossRef](#)]
19. Liu, W.; Zhong, Z.; Hu, N.; Zhou, Y.; Maggio, L.; Miri, A.K.; Fragasso, A.; Jin, X.; Khademhosseini, A.; Zhang, Y.S. Coaxial extrusion bioprinting of 3D microfibrillar constructs with cell-favorable gelatin methacryloyl microenvironments. *Biofabrication* **2017**, *10*, 024102. [[CrossRef](#)] [[PubMed](#)]
20. Chedly, J.; Soares, S.; Montembault, A.; von Boxberg, Y.; Veron-Ravaille, M.; Mouffle, C.; Benassy, M.-N.; Taxi, J.; David, L.; Nothias, F. Physical chitosan microhydrogels as scaffolds for spinal cord injury restoration and axon regeneration. *Biomaterials* **2017**, *138*, 91–107. [[CrossRef](#)]
21. Doench, I.; Tran, T.A.; David, L.; Montembault, A.; Viguier, E.; Gorzelanny, C.; Sudre, G.; Cachon, T.; Louback-Mohamed, M.; Horbelt, N.; et al. Cellulose nanofiber-reinforced chitosan hydrogel composites for intervertebral disc tissue repair. *Biomimetics* **2019**, *4*, 19. [[CrossRef](#)] [[PubMed](#)]
22. Doench, I.; Torres-Ramos, M.E.W.; Montembault, A.; De Oliveira, P.N.; Halimi, C.; Viguier, E.; Heux, L.; Siadous, R.; Thiré, R.M.S.M.; Osorio-Madrado, A. Injectable and gellable chitosan formulations filled with cellulose nanofibers for intervertebral disc tissue engineering. *Polymers* **2018**, *10*, 1202. [[CrossRef](#)] [[PubMed](#)]
23. Fiamingo, A.; Montembault, A.; Boitard, S.-E.; Naemetalla, H.; Agbulut, O.; Delair, T.; Campana-Filho, S.P.; Menasché, P.; David, L. Chitosan hydrogels for the regeneration of infarcted myocardium: Preparation, physicochemical characterization, and biological evaluation. *Biomacromolecules* **2016**, *17*, 1662–1672. [[CrossRef](#)] [[PubMed](#)]
24. Rami, L.; Malaise, S.; Delmond, S.; Fricain, J.-C.; Siadous, R.; Schlaubitz, S.; Laurichesse, E.; Amedee, J.; Montembault, A.; David, L.; et al. Physicochemical modulation of chitosan-based hydrogels induces different biological responses: Interest for tissue engineering. *J. Biomed. Mater. Res. Part A* **2013**, *102*, 3666–3676. [[CrossRef](#)] [[PubMed](#)]
25. Ladet, S.; Tahiri, K.; Montembault, A.; Domard, A.; Corvol, M.-T. Multi-membrane chitosan hydrogels as chondrocytic cell bioreactors. *Biomaterials* **2011**, *32*, 5354–5364. [[CrossRef](#)]
26. De Souza, R.F.B.; De Souza, F.C.B.; Rodrigues, C.; Drouin, B.; Papat, K.C.; Mantovani, D.; Moraes, Â.M. Mechanically-enhanced polysaccharide-based scaffolds for tissue engineering of soft tissues. *Mater. Sci. Eng. C* **2019**, *94*, 364–375. [[CrossRef](#)]
27. García, D.E.; Glasser, W.G.; Pizzi, T.A.; Osorio-Madrado, A.; Laborie, M.-P.G. Synthesis and physicochemical properties of hydroxypropyl tannins from maritime pine bark (*Pinus pinaster* Ait.). *Holzforchung* **2014**, *68*, 411–418. [[CrossRef](#)]
28. Osorio Madrado, A. Whiskers of chitosan for bio-nano-composites. Ph.D. Thesis, Laboratoire Ingénierie des Matériaux Polymères IMP, Claude Bernard University Lyon 1, Villeurbanne, France, 2008.
29. Agüero, H.P.; David, L.; Covas, C.P.; Osorio-Madrado, A. Bioinspired chitosan-BSA fibers for applications in tissue engineering of the fibrous ring of intervertebral discs. *Rev. Cuba. Investig. Bioméd.* **2017**, *36*, 1–11.
30. Peniche, H.; Osorio, A.; Acosta, N.; De La Campa, A.; Peniche, C. Preparation and characterization of superparamagnetic chitosan microspheres: Application as a support for the immobilization of tyrosinase. *J. Appl. Polym. Sci.* **2005**, *98*, 651–657. [[CrossRef](#)]
31. Toeri, J.; Osorio-Madrado, A.; Laborie, M.-P. Preparation and chemical/microstructural characterization of azacrown ether-crosslinked chitosan films. *Materials* **2017**, *10*, 400. [[CrossRef](#)]
32. Von Palubitzki, L.; Wang, Y.; Hoffmann, S.; Vidal-Y-Sy, S.; Zobiak, B.; Failla, A.V.; Schmage, P.; John, A.; Osorio-Madrado, A.; Bauer, A.T.; et al. Differences of the tumour cell glycoalyx affect binding of capsaicin-loaded chitosan nanocapsules. *Sci. Rep.* **2020**, *10*, 1–16. [[CrossRef](#)] [[PubMed](#)]
33. Osorio, A.; Trombotto, S.; Lucas, J.-M.; Peniche, C.; David, L.; Domard, A. Solid-state acid hydrolysis of chitosan: Evolution of the crystallinity and the macromolecular structure. In Proceedings of the 10th International Conference on Chitin and Chitosan, 7th International Conference of the European Chitin Society, Montpellier, France, 6–9 September 2006; pp. 609–615.
34. Gorzelanny, C.; Pöppelmann, B.; Pappelbaum, K.; Moerschbacher, B.M.; Schneider, S.W. Human macrophage activation triggered by chitotriosidase-mediated chitin and chitosan degradation. *Biomaterials* **2010**, *31*, 8556–8563. [[CrossRef](#)] [[PubMed](#)]
35. Mathews, S.; Gupta, P.K.; Bhonde, R.; Totey, S. Chitosan enhances mineralization during osteoblast differentiation of human bone marrow-derived mesenchymal stem cells, by upregulating the associated genes. *Cell Prolif.* **2011**, *44*, 537–549. [[CrossRef](#)] [[PubMed](#)]
36. Deng, Y.; Ren, J.; Chen, G.; Li, G.; Wu, X.; Wang, G.; Gu, G.; Li, J. Injectable in situ cross-linking chitosan-hyaluronic acid based hydrogels for abdominal tissue regeneration. *Sci. Rep.* **2017**, *7*, 1–13. [[CrossRef](#)] [[PubMed](#)]
37. Chatelet, C.; Damour, O.; Domard, A. Influence of the degree of acetylation on some biological properties of chitosan films. *Biomaterials* **2001**, *22*, 261–268. [[CrossRef](#)]

38. Montebault, A.; Tahiri, K.; Korwin-Zmijowska, C.; Chevalier, X.; Corvol, M.-T.; Domard, A. A material decoy of biological media based on chitosan physical hydrogels: Application to cartilage tissue engineering. *Biochimie* **2006**, *88*, 551–564. [[CrossRef](#)] [[PubMed](#)]
39. Osorio-Madrado, A.; Eder, M.; Rueggeberg, M.; Pandey, J.K.; Harrington, M.J.; Nishiyama, Y.; Putaux, J.-L.; Rochas, C.; Burgert, I. Reorientation of cellulose nanowhiskers in agarose hydrogels under tensile loading. *Biomacromolecules* **2012**, *13*, 850–856. [[CrossRef](#)]
40. Osorio-Madrado, A.; David, L.; Covas, C.A.P.; Rochas, C.; Putaux, J.-L.; Trombotto, S.; Alcouffe, P.; Domard, A. Fine microstructure of processed chitosan nanofibril networks preserving directional packing and high molecular weight. *Carbohydr. Polym.* **2015**, *131*, 1–8. [[CrossRef](#)]
41. Osorio-Madrado, A.; David, L.; Trombotto, S.; Lucas, J.-M.; Covas, C.A.P.; Domard, A. Highly crystalline chitosan produced by multi-steps acid hydrolysis in the solid-state. *Carbohydr. Polym.* **2011**, *83*, 1730–1739. [[CrossRef](#)]
42. Samyn, P.; Osorio-Madrado, A. Native crystalline polysaccharide nanofibers: Processing and properties. In *Handbook of Nanofibers*; Barhoum, A., Bechelany, M., Makhoulouf, A., Eds.; Springer International Publishing: Cham, Germany, 2018; pp. 1–36.
43. Osorio-Madrado, A.; Laborie, M.P. Morphological and thermal investigations of cellulosic bionanocomposites. In *Biopolymer Nanocomposites*; Dufresne, A., Thomas, S., Pothen, L.A., Eds.; John Wiley & Sons, Inc.: Hoboken, NJ, USA, 2013; pp. 411–435.
44. Mao, J.; Osorio-Madrado, A.; Laborie, M.-P. Preparation of cellulose I nanowhiskers with a mildly acidic aqueous ionic liquid: Reaction efficiency and whiskers attributes. *Cellulose* **2013**, *20*, 1829–1840. [[CrossRef](#)]
45. Favier, V.; Chanzy, H.; Cavaille, J.Y. Polymer nanocomposites reinforced by cellulose whiskers. *Macromolecules* **1995**, *28*, 6365–6367. [[CrossRef](#)]
46. Marquez-Bravo, S.; Doench, I.; Molina, P.; Bentley, F.; Tamo, A.; Passieux, R.; Lossada, F.; David, L.; Osorio-Madrado, A. Functional bionanocomposite fibers of chitosan filled with cellulose nanofibers obtained by gel spinning. *Polymers* **2021**, *13*, 1563. [[CrossRef](#)]
47. Klemm, D.; Kramer, F.; Moritz, S.; Lindström, T.; Ankerfors, M.; Gray, D.; Dorris, A. Nanocelluloses: A new family of nature-based materials. *Angew. Chem. Int. Ed.* **2011**, *50*, 5438–5466. [[CrossRef](#)] [[PubMed](#)]
48. Abushammala, H.; Pontes, J.F.; Gomes, G.H.M.; Osorio-Madrado, A.; Thiré, R.M.; Pereira, F.V.; Laborie, M.-P.G. Swelling, viscoelastic, and anatomical studies on ionic liquid-swollen Norway spruce as a screening tool toward ionosolv pulping. *Holzforschung* **2015**, *69*, 1059–1067. [[CrossRef](#)]
49. Mao, J.; Osorio-Madrado, A.; Laborie, M.-P. Novel preparation route for cellulose nanowhiskers. In *Abstracts of Papers of the American Chemical Society*; American Chemical Society: Washington, DC, USA, 2013.
50. Kovacs, T.; Naish, V.; O'Connor, B.; Blaise, C.; Gagné, F.; Hall, L.; Trudeau, V.; Martel, P. An ecotoxicological characterization of nanocrystalline cellulose (NCC). *Nanotoxicology* **2010**, *4*, 255–270. [[CrossRef](#)] [[PubMed](#)]
51. Pitkänen, M.; Honkalampi, U.; Von Wright, A.; Sneck, A.; Hentze, H.P.; Sievänen, J.; Hiltunen, J.; Hellen, E. Nanofibrillar cellulose: In vitro study of cytotoxic and genotoxic properties. In Proceedings of the International Conference on Nanotechnology for the Forest Products Industry, Espoo, Finland, 27–29 September 2010.
52. Pértile, R.A.; Moreira, S.; Gil Da Costa, R.M.; Correia, A.; Guãrdao, L.; Gärtner, M.D.F.; Vilanova, M.; Gama, M. Bacterial cellulose: Long-Term biocompatibility studies. *J. Biomater. Sci. Polym. Ed.* **2012**, *23*, 1339–1354. [[CrossRef](#)]
53. Kolakovic, R.; Laaksonen, T.; Peltonen, L.; Laukkanen, A.; Hirvonen, J. Spray-dried nanofibrillar cellulose microparticles for sustained drug release. *Int. J. Pharm.* **2012**, *430*, 47–55. [[CrossRef](#)]
54. Eyholzer, C.; De Couraça, A.B.; Duc, F.; Bourban, P.E.; Tingaut, P.; Zimmermann, T.; Månson, J.A.E.; Oksman, K. Biocomposite hydrogels with carboxymethylated, nanofibrillated cellulose powder for replacement of the nucleus pulposus. *Biomacromolecules* **2011**, *12*, 1419–1427. [[CrossRef](#)]
55. Borges, A.C.; Eyholzer, C.; Duc, F.; Bourban, P.-E.; Tingaut, P.; Zimmermann, T.; Pioletti, D.P.; Månson, J.-A.E. Nanofibrillated cellulose composite hydrogel for the replacement of the nucleus pulposus. *Acta Biomater.* **2011**, *7*, 3412–3421. [[CrossRef](#)]
56. Tamo, A.K.; Doench, I.; Helguera, A.M.; Hoenders, D.; Walther, A.; Osorio-Madrado, A. Biodegradation of crystalline cellulose nanofibers by means of enzyme immobilized-alginate beads and microparticles. *Polymers* **2020**, *12*, 1522. [[CrossRef](#)]
57. Arola, S.; Tammelin, T.; Setälä, H.; Tullila, A.; Linder, M.B. Immobilization–stabilization of proteins on nanofibrillated cellulose derivatives and their bioactive film formation. *Biomacromolecules* **2012**, *13*, 594–603. [[CrossRef](#)] [[PubMed](#)]
58. De France, K.J.; Hoare, T.; Cranston, E.D. Review of hydrogels and aerogels containing nanocellulose. *Chem. Mater.* **2017**, *29*, 4609–4631. [[CrossRef](#)]
59. Osorio-Madrado, A.; David, L.; Montebault, A.; Viguier, E.; Cachon, T. Hydrogel composites comprising chitosan and cellulose nanofibers. US Patent Application 16/980383, 18 February 2021.
60. Osorio-Madrado, A.; Fratzl, P.; David, L.; Urban, G.; Montebault, A.; Crepet, A.; Gorzelanny, C.; Mochales-Palau, C.; Heux, L.; Putaux, J.-L.; et al. Synthese und Charakterisierung von Biomaterialien (Polymere, Metalle, Keramiken, Komposite). P85: Hydrogel nanocomposite biomaterials for intervertebral disc tissue engineering. Preparation, characterization and application. *Bionanomaterials* **2015**, *16*, 236–255. [[CrossRef](#)]
61. Omlor, G.W.; Nerlich, A.G.; Lorenz, H.; Bruckner, T.; Richter, W.; Pfeiffer, M.; Gühring, T. Injection of a polymerized hyaluronic acid/collagen hydrogel matrix in an in vivo porcine disc degeneration model. *Eur. Spine J.* **2012**, *21*, 1700–1708. [[CrossRef](#)]
62. Endres, M.; Abbushi, A.; Thomale, U.W.; Cabraja, M.; Kroppenstedt, S.N.; Morawietz, L.; Casalis, P.A.; Zenclussen, M.L.; Lemke, A.-J.; Horn, P.; et al. Intervertebral disc regeneration after implantation of a cell-free bioresorbable implant in a rabbit disc degeneration model. *Biomaterials* **2010**, *31*, 5836–5841. [[CrossRef](#)]

63. Hegewald, A.A.; Knecht, S.; Baumgartner, D.; Gerber, H.; Endres, M.; Kaps, C.; Stüssi, E.; Thomé, C. Biomechanical testing of a polymer-based biomaterial for the restoration of spinal stability after nucleotomy. *J. Orthop. Surg. Res.* **2009**, *4*, 1–9. [[CrossRef](#)]
64. Nakashima, S.; Matsuyama, Y.; Takahashi, K.; Satoh, T.; Koie, H.; Kanayama, K.; Tsuji, T.; Maruyama, K.; Imagama, S.; Sakai, Y.; et al. Regeneration of intervertebral disc by the intradiscal application of cross-linked hyaluronate hydrogel and cross-linked chondroitin sulfate hydrogel in a rabbit model of intervertebral disc injury. *Bio. Med. Mater. Eng.* **2009**, *19*, 421–429. [[CrossRef](#)]
65. Rennerfeldt, D.A.; Renth, A.N.; Talata, Z.; Gehrke, S.H.; Detamore, M.S. Tuning mechanical performance of poly(ethylene glycol) and agarose interpenetrating network hydrogels for cartilage tissue engineering. *Biomaterials* **2013**, *34*, 8241–8257. [[CrossRef](#)]
66. Chou, A.I.; Nicoll, S.B. Characterization of photocrosslinked alginate hydrogels for nucleus pulposus cell encapsulation. *J. Biomed. Mater. Res. Part A* **2009**, *91*, 187–194. [[CrossRef](#)]
67. Varma, D.; Lin, H.; Long, R.; Gold, G.; Hecht, A.; Iatridis, J.; Nicoll, S. Thermoresponsive, redox-polymerized cellulosic hydrogels undergo in situ gelation and restore intervertebral disc biomechanics post discectomy. *Eur. Cells Mater.* **2018**, *35*, 300–317. [[CrossRef](#)]
68. Sharifi, S.; Bulstra, S.K.; Grijpma, D.W.; Kuijjer, R. Treatment of the degenerated intervertebral disc; closure, repair and regeneration of the annulus fibrosus. *J. Tissue Eng. Regen. Med.* **2014**, *9*, 1120–1132. [[CrossRef](#)] [[PubMed](#)]
69. Hirai, A.; Odani, H.; Nakajima, A. Determination of degree of deacetylation of chitosan by ¹H NMR spectroscopy. *Polym. Bull.* **1991**, *26*, 87–94. [[CrossRef](#)]
70. Lall, A.; Tamo, A.K.; Doench, I.; David, L.; De Oliveira, P.N.; Gorzelanny, C.; Osorio-Madrado, A. Nanoparticles and colloidal hydrogels of chitosan-caseinate polyelectrolyte complexes for drug-controlled release applications. *Int. J. Mol. Sci.* **2020**, *21*, 5602. [[CrossRef](#)]
71. Osorio-Madrado, A.; David, L.; Trombotto, S.; Lucas, J.-M.; Covas, C.A.P.; Domard, A. Kinetics study of the solid-state acid hydrolysis of chitosan: Evolution of the crystallinity and macromolecular structure. *Biomacromolecules* **2010**, *11*, 1376–1386. [[CrossRef](#)] [[PubMed](#)]
72. Lamarque, G.; Viton, C.; Domard, A. Comparative study of the first heterogeneous deacetylation of α - and β -chitins in a multistep process. *Biomacromolecules* **2004**, *5*, 992–1001. [[CrossRef](#)] [[PubMed](#)]
73. Sorlier, P.; Denuzière, A.; Viton, C.; Domard, A. Relation between the degree of acetylation and the electrostatic properties of chitin and chitosan. *Biomacromolecules* **2001**, *2*, 765–772. [[CrossRef](#)]
74. Pääkkö, M.; Ankerfors, M.; Kosonen, H.; Nykänen, A.; Ahola, S.; Österberg, M.; Ruokolainen, J.; Laine, J.; Larsson, P.T.; Ikkala, O.; et al. Enzymatic hydrolysis combined with mechanical shearing and high-pressure homogenization for nanoscale cellulose fibrils and strong gels. *Biomacromolecules* **2007**, *8*, 1934–1941. [[CrossRef](#)]
75. Schindelin, J.; Arganda-Carreras, I.; Frise, E.; Kaynig, V.; Longair, M.; Pietzsch, T.; Preibisch, S.; Rueden, C.; Saalfeld, S.; Schmid, B.; et al. Fiji: An open-source platform for biological-image analysis. *Nat. Methods* **2012**, *9*, 676–682. [[CrossRef](#)]
76. Arganda-Carreras, I.; Kaynig, V.; Rueden, C.; Eliceiri, K.W.; Schindelin, J.E.; Cardona, A.; Seung, H.S. Trainable Weka Segmentation: A machine learning tool for microscopy pixel classification. *Bioinformatics* **2017**, *33*, 2424–2426. [[CrossRef](#)]
77. Graessley, W.W. *The Entanglement Concept in Polymer Rheology*; Springer Science and Business Media LLC: Berlin, Germany, 2006; pp. 1–179.
78. Hwang, J.K.; Shin, H.H. Rheological properties of chitosan solutions. *Korea Aust. Rheol. J.* **2000**, *12*, 175–179.
79. Cross, M.M. Rheology of non-Newtonian fluids: A new flow equation for pseudoplastic systems. *J. Colloid Sci.* **1965**, *20*, 417–437. [[CrossRef](#)]
80. Calero, N.; Muñoz, J.; Ramírez, P.; Guerrero, A. Flow behaviour, linear viscoelasticity and surface properties of chitosan aqueous solutions. *Food Hydrocoll.* **2010**, *24*, 659–666. [[CrossRef](#)]
81. Halimi, C.; Montembault, A.; Guerry, A.; Delair, T.; Viguier, E.; Fulchiron, R.; David, L. Chitosan solutions as injectable systems for dermal filler applications: Rheological characterization and biological evidence. In Proceedings of the 2015 37th Annual International Conference of the IEEE Engineering in Medicine and Biology Society (EMBC), Milano, Italy, 25–29 August 2015; pp. 2596–2599.
82. Montembault, A.; Viton, C.; Domard, A. Rheometric study of the gelation of chitosan in a hydroalcoholic medium. *Biomaterials* **2005**, *26*, 1633–1643. [[CrossRef](#)] [[PubMed](#)]
83. Montembault, A.; Viton, A.C.; Domard, A. Rheometric study of the gelation of chitosan in aqueous solution without cross-linking agent. *Biomacromolecules* **2005**, *6*, 653–662. [[CrossRef](#)] [[PubMed](#)]
84. Kienzle-Sterzer, C.; Rodríguez-Sánchez, D.; Rha, C. Flow behavior of a cationic biopolymer: Chitosan. *Polym. Bull.* **1985**, *13*, 1–6. [[CrossRef](#)]
85. Foster, E.J.; Moon, R.J.; Agarwal, U.P.; Bortner, M.J.; Bras, J.; Camarero-Espinosa, S.; Chan, K.J.; Clift, M.J.D.; Cranston, E.D.; Eichhorn, S.J.; et al. Current characterization methods for cellulose nanomaterials. *Chem. Soc. Rev.* **2018**, *47*, 2609–2679. [[CrossRef](#)]
86. Gharehkhani, S.; Sadeghinezhad, E.; Kazi, S.N.; Yarmand, H.; Badarudin, A.; Safaei, M.R.; Zubir, M.N.M. Basic effects of pulp refining on fiber properties—A review. *Carbohydr. Polym.* **2015**, *115*, 785–803. [[CrossRef](#)]
87. Tanaka, R.; Saito, T.; Hondo, H.; Isogai, A. Influence of flexibility and dimensions of nanocelluloses on the flow properties of their aqueous dispersions. *Biomacromolecules* **2015**, *16*, 2127–2131. [[CrossRef](#)]
88. Falcoz-Vigne, L.; Ogawa, Y.; Molina-Boisseau, S.; Nishiyama, Y.; Meyer, V.; Petit-Conil, M.; Mazeau, K.; Heux, L. Quantification of a tightly adsorbed monolayer of xylan on cellulose surface. *Cellulose* **2017**, *24*, 3725–3739. [[CrossRef](#)]

89. Toivonen, M.S.; Kurki-Suonio, S.; Schacher, F.H.; Hietala, S.; Rojas, O.; Ikkala, O. Water-resistant, transparent hybrid nanopaper by physical cross-linking with chitosan. *Biomacromolecules* **2015**, *16*, 1062–1071. [[CrossRef](#)]
90. Haider, S.; Al-Zeghayer, Y.; Ali, F.A.A.; Haider, A.; Mahmood, A.; Al-Masry, W.A.; Imran, M.; Aijaz, M.O. Highly aligned narrow diameter chitosan electrospun nanofibers. *J. Polym. Res.* **2013**, *20*, 1–11. [[CrossRef](#)]
91. Robitzer, M.; David, L.; Rochas, C.; Di Renzo, F.; Quignard, F. Supercritically-dried alginate aerogels retain the fibrillar structure of the hydrogels. *Macromol. Symp.* **2008**, *273*, 80–84. [[CrossRef](#)]
92. Sereni, N.; Enache, A.; Sudre, G.; Montembault, A.; Rochas, C.; Durand, P.; Perrard, M.-H.; Bozga, G.; Puaux, J.-P.; Delair, T.; et al. Dynamic structuration of physical chitosan hydrogels. *Langmuir* **2017**, *33*, 12697–12707. [[CrossRef](#)] [[PubMed](#)]
93. Robitzer, M.; David, L.; Rochas, C.; Di Renzo, F.; Quignard, F. Nanostructure of calcium alginate aerogels obtained from multistep solvent exchange route. *Langmuir* **2008**, *24*, 12547–12552. [[CrossRef](#)] [[PubMed](#)]
94. Wang, H.; Xu, J.; Sun, S.; Liu, Y.; Zhu, C.; Li, J.; Sun, J.; Wang, S.; Zhang, H. Characterization of crystal microstructure based on small angle X-ray scattering (SAXS) Technique. *Molecules* **2020**, *25*, 443. [[CrossRef](#)] [[PubMed](#)]
95. Crawford, S.M.; Kolsky, H. Stress birefringence in polyethylene. *Proc. Phys. Soc. Sect. B* **1951**, *64*, 119–125. [[CrossRef](#)]
96. Boote, C.; Sturrock, E.J.; Attenburrow, G.E.; Meek, K.M. Pseudo-affine behaviour of collagen fibres during the uniaxial deformation of leather. *J. Mater. Sci.* **2002**, *37*, 3651–3656. [[CrossRef](#)]